Submitted to the Special Issue on 'Trends in Polymer Nanocomposite Materials'

Review

Ductility, toughness and strain recovery in self-healing dual cross-linked nanoparticle networks studied by computer simulations

Balaji V. S. Iyer,[a] Victor V. Yashin,[a] Matthew J. Hamer,[a]
Tomasz Kowalewski,[b] Krzysztof Matyjaszewski[b] and Anna C. Balazs[a,]*
[a]*Chemical Engineering Department, University of Pittsburgh, Pennsylvania 15261, USA*
[b]*Department of Chemistry, Carnegie Mellon University, Pennsylvania 15213, USA*

ABSTRACT

One of the challenges in formulating useful nanocomposites is creating materials that are both tough and strong. Here, we review results of computational studies on a new class of nanocomposites that exhibit these desirable properties. The fundamental unit in these materials is a polymer grafted nanoparticle (PGN), which encompasses a rigid core and a corona of end-grafted polymers. We focus on a concentrated solution of these PGNs; the solution is assumed to be a good solvent for the grafted chains, which are in the semi-dilute regime. The free ends of the grafted chains encompass chemically reactive groups. Hence, with the overlap of the coronas on neighboring nanoparticles, the reactive end groups can form labile or more stable ("permanent") bonds, leading to the creation of a "dual cross-linked" network. To predict the mechanical properties of these dual cross-linked PGN networks, we developed a multi-scale model that captures interactions occurring over the range of length and time scales that characterize the performance of the system. Namely, the model integrates the essential structural features of the polymer grafted nanoparticles, the interactions between the overlapping coronas, the kinetics of bond formation and rupture between the reactive end-groups and the response of the entire sample to mechanical deformation. Using this computational approach, we determined the effect of the labile bond energy, the fraction of permanent bonds and the introduction of high-strength bonds on the ductility and toughness of the PGN network. Furthermore, we determined the strain recovery and self-healing behavior of the material after it was allowed to relax from an applied tensile force. Through these studies, we isolated critical parameters that control the mechanical response and rejuvenation of dual cross-linked PGN networks. Our findings allow researchers to understand how variations in these key parameters can lead to changes in the materials' mechanical behavior and thus, can facilitate the fabrication of the next generation of nanocomposites with novel and technologically useful properties.

Keywords: Dual cross-linked networks, polymer grafted nanoparticles, self-healing nanocomposites, strain recovery.

*Corresponding author.

E-mail address: balazs@pitt.edu (A.C.Balazs)

1. Introduction

A diverse array of animals, from fish, reptiles and some mammals, can respond to predators by morphing their skin into a protective "armor" that shields them from harm.[1] The advent of adaptive synthetic materials that dynamically form an analogous armor would significantly extend the lifetime and sustainability of manufactured goods. Namely, it would be highly beneficial to design coatings that respond to mechanical impact by self-organizing into a strong, tough layer that shields the underlying material from damage. Natural armor, such as the armadillo's shell, can provide useful design concepts for the fabrication of such adaptive coatings. Notably, the armadillo's skin encompasses two salient features.[1] First, the animal's outer skin is composed of rigid segments that are interconnected by soft biopolymers; these soft components impart the structure with vital flexibility and a means of absorbing and dissipating energy. Second, the entire dermal armor encompasses a complex hierarchical structure, providing reinforcement over a range of length scales. Based on the performance of the armadillo's skin, it could be argued that flexibility and structural hierarchy are key components for creating synthetic materials that can emulate the desirable properties of natural armor.

Here, we describe our recent computational studies [2-4] on designing materials that encompass these fundamental elements and thus, exhibit remarkable strength and toughness in response to mechanical deformation. As in the above example, our system contains both hard and soft components; the fundamental unit is a hard, spherical nanoparticle that is coated with end-grafted polymers, which constitute the soft component. This entire unit is referred to as a polymer-grafted nanoparticle or PGN. Importantly, the free ends of the grafted polymers contain chemically reactive groups, which bind the PGNs into a macroscopic network. Figure 1 illustrates these different components and highlights the hierarchical structure of the material.

Place Figure 1 here.

As seen at the top of Fig. 1, the reactive end groups constitute the smallest length scale in the system. These species enable the polymer "arms" on neighboring PGNs to form either weak, labile bonds, which readily reform after they have broken, or stronger, more "permanent" bonds, which are less chemically reactive and thus, do not reform after they are ruptured. At this length scale, our model details the kinetics of bond formation and rupture between the reactive end groups. At the next, larger length scale, the model describes the polymeric corona surrounding the nanoparticles, capturing the interactions between neighboring coronas. The interconnected macroscopic sample forms the largest length scale in the system and at this length scale, the model describes the global response of the network to an applied force. As will be seen below, the components of this system are highly integrated, so that the rupture and formation of bonds between the reactive end groups controls the response of the entire sample to large-scale deformation and imbues the material with superior mechanical properties.

In these studies, we specifically focused on PGN networks prepared by cross-linking a concentrated solution of PGNs; the solution is assumed to be a good solvent for the grafted chains, which are in the semi-dilute regime. After cross-linking, the system behaves as a soft solid. The presence of the solvent makes these composites relatively new materials;[5,6] previous experimental studies involving interconnected, coated nanoparticles focused primarily on neat systems or those mixed with free polymer chains.[7-15] The solvent in such systems facilitates the motion of the chains and nanoparticles that, in turn, enables the material to dynamically reconfigure in response to the deformations. As indicated above, the particles are bound by both labile and permanent bonds and thus, we say that the system displays "dual cross-linking". In this respect, the PGN networks resemble the double-network gels,[16,17] which involve both strong and weak connections to enhance the strength and toughness of the materials. On the other hand, the double-network gels involve a distinct topology, which consists of interpenetrating networks of stronger and weaker chains that are cross-linked randomly and break irreversibly.[18,19] Thus, these gels are quite different from the networks considered here.

Below, we first summarize our multi-scale computational approach for modeling the PGN networks and then discuss the specific studies we undertook to optimize the design of composites that show a remarkable ability to recover from mechanical deformation. In particular, we first examine how the energies of the labile bonds and the fraction of permanent bonds affect the response of the materials to tensile deformation. With this information in hand, we then examine how the system responds when the applied force is released and thereby determine the optimal conditions for achieving maximal recovery of the materials properties.

2. Modeling polymer grafted nanoparticle networks

2.1. Theoretical and computational approach

In our model for the dual cross-linked PGNs,[2-4] the individual nanoparticles are composed of a rigid core of radius r_0 and a corona of grafted polymers whose thickness is given by $H = qr_0$. To capture the interactions in this system, our model integrates the essential structural characteristics of the polymer-grafted nanoparticles, the interactions between the overlapping coronas, and the kinetics of bond formation and rupture between the reactive groups on the chain ends. Here, we provide a brief description of this multi-scale approach. The length scales in the ensuing discussion are given with respect to the core radius r_0 and hence, a PGN has a core radius of unity and corona thickness q.

The interaction between two PGNs is described by a sum of energy potentials $U_{int} = U_{rep} + U_{coh} + U_{link}$. The first term characterizes the repulsive interactions between the coated spherical particles in a good solvent. We assume that the repulsion between the particles is due solely to the interaction between the thickly grafted corona chains. At a small degree of overlap between the coronas, the repulsion between two PGNs is similar to that between two multi-arm star polymers having the same size and number of arms as the PGNs. Thus, we describe the repulsion between the coated particles through the effective interaction potential between multi-arm star polymers given by:[20,21]

$$\frac{U_{rep}(R)}{k_B T} = \frac{5}{18} f^{3/2} \times \begin{cases} -\ln(R/\sigma) + (1 + f^{1/2}/2)^{-1} & , R \le \sigma \\ (1 + f^{1/2}/2)^{-1}(\sigma/R)\exp[-f^{1/2}(R-\sigma)/2\sigma] & , R > \sigma \end{cases} \tag{1}$$

Here, f is the number of arms, R is the center-to-center inter-particle separation and $\sigma = 2(1+q)(1+2f^{-1/2})^{-1}$ is the range [21,22] of the potential. The attractive cohesive interaction between the coated nanoparticles is described by a pseudo-potential $U_{coh}(R)$, which is constant for small values of R and balances the repulsion at the corona edges to allow for overlap between neighboring coronas.[23] It is chosen to have the following form,[23]:

$$U_{coh}(R) = -C\{1 + \exp[(R - A)/B]\}^{-1} \tag{2}$$

where C is an energy scale, and A and B are length scales that determine the respective location and width of the attractive well in the potential. Notably, the shape of this potential well has a flat bottom and smooth wall.

The term U_{link} describes the attractive interaction between the particles linked by the bonded polymer arms. The attractive force acting between the two bonded particles is:

$$F_{link}(r) = N_b \kappa(r)\, r \tag{3}$$

where N_b is the number of bonds formed between the given pair of particles, and $\kappa(r)$ is the spring stiffness, which increases progressively with the chain end-to-end distance $r = R - 2$. We use the following equation, obtained for a worm-like chain[24], to calculate $\kappa(r)$:

$$\kappa(r) = k_B T\, R_0^{-2}\{1 + 2[1 - r^2(2L)^{-2}]^{-2}\} \tag{4}$$

Here, $2L$ is the contour length of the chain formed by bonding two polymer arms of length L, $R_0^2 = 4l_p L$ is the mean-square end-to-end distance of the latter chain, and l_p is its persistence length.[24] At small deformations $r << 2L$, eq. (4) gives the spring constant of a Gaussian chain: $\kappa(r) \approx 3k_B T R_0^{-2}$. The chain stiffens significantly ($\kappa(r)$ increases noticeably) when r becomes comparable to $2L$ (see eq. (4)).

The value of N_b in eq. (3) depends on the extent of overlap between the coronas of the nanoparticles, and on the kinetics of bond formation and rupture.[2-4] We use the Bell model [25-28] to describe the rupture and reformation of individual bonds. In our model, both the permanent (*p*) and labile (*l*) bonds can rupture, but only the labile bonds can reform after they are ruptured. The rupture rate increases when the force F is applied to the bond, so that $k_r^{(p,l)} = k_{0r}^{(p,l)} \exp(\gamma_0 F)$,[25-28] where $k_{0r}^{(p,l)} = \nu^{(p,l)} \exp(-U_0^{(p,l)} / k_B T)$ is the rupture rate at no force, and $U_0^{(p,l)}$ is the bond energy. For reversible bond formation in the zero force limit, the ratio of the formation to rupture rate is given by $k_{0f}^{(l)} / k_{0r}^{(l)} = \exp(U_0^{(l)} / k_B T)$.[26,27] In general, the rate constant of bond formation decreases under an applied force.[28] For simplicity, we neglect the dependence of the rate constant of bond formation on force and consider it to be constant, $k_{0f}^{(l)}$.[2-4]

The evolution of the number of bonds is described by:[2-4]

$$\frac{dN_b}{dt} = -k_r(R)N_b + P_c(R)k_f(R)[N_{max}(R) - N_b]^2 \ . \tag{5}$$

where $N_{max}(R)$ is the maximal number of bonds that can be formed between two nanoparticles at the center-to-center distance R, and $P_c(R)$ is the probability of contact of two chain ends. For a single polymer arm, the probability p to have a bond with an arm belonging to a neighboring PGN is described by an equation similar to eq. (5):

$$\frac{dp}{dt} = -k_r(R)p + P_c(R)k_f(R)[N_{max}(R) - N_b](1-p) \ . \tag{6}$$

At a given R, both $N_{max}(R)$ and $P_c(R)$ depend on the number of grafted chains per particle f and the corona thickness q. We make the simplifying assumption that there is negligible distortion of the two coronas when they overlap. Then, purely geometric considerations are used to determine the value of $N_{max}(R)$.[2-4]

The probability of contact between chain ends, $P_c(R)$, depends on the free-end distribution in the corona of the spherical PGNs that is characterized by the distribution function $g(r)$, with r being the distance from the particle center. The function $P_c(R)$ is calculated by numerical integration of the product of the individual free-end distributions in each corona over the volume of overlap, i.e., $P_c(R) = \int_{overlap} g(|\mathbf{R} - \mathbf{r}|)\, g(|\mathbf{r}|)\, d\mathbf{r}$. We use the expression for $g(r)$ obtained from self-consistent field theory for a single spherical PGN in a good solvent.[29] The same self-consistent field theory is used to determine the contour length L at given values of nanoparticle radius r_0, number of grafted arms f, and corona thickness $H = q\, r_0$.[2-4]

The dynamics of the system is assumed to be in the overdamped regime, with the equation of motion of each particle being: $d\mathbf{x}/dt = \mu \mathbf{F}_{tot}$, where μ is the mobility and $\mathbf{F}_{tot}$ is the total force on the polymer-grafted particle. Here, $\mathbf{F}_{tot} = -\partial U_{int} / \partial \mathbf{x} + \mathbf{F}_{ext}$, where $\mathbf{F}_{ext}$ is the external force acting on the edge particles of the particle array. The equation of motion is solved numerically in two steps since the polymer spring force within $\mathbf{F}_{tot}$ depends on the number of bonds between particles. In the first step, we determine the number of bonds at any given time, $N_b(t)$, by numerically evolving eq. (5) through an explicit Euler scheme. Note that the numerical evolution of eq. (5) yields a real number, whereas the number of bonds $N_b(t)$ should take discrete integer values. In order to determine the integer value, we compare the fractional part of the numerical result, $\{N_b(t)\}$, with a random number ξ distributed uniformly between 0 and 1. If $\{N_b(t)\} < \xi$, then we truncate the result; otherwise, we increment the integer part of the result by 1. In the second step, we use this value to calculate the spring force (see eq. (3)) in the above equation of motion and then numerically integrate this dynamic equation using a fourth-order Runge-Kutta algorithm.

2.2. Initial setup and model parameters

The equations describe three-dimensional spherical nanoparticles with a 3D corona of chains. We solved these equations in 2D, representing a plane through this material. The initial state of the system is generated using the following five-step procedure. In the first step, the nanoparticles are placed in an array such that their centers are separated by a horizontal spacing of $1.8(1+q)$ and a vertical spacing of $1.62(1+q)$, with a horizontal offset position of $0.855(1+q)$ between adjacent rows. In the second step, we hold the sample in the initial configuration for $4\times10^3 T_0$ units of time to allow for the formation of the labile bonds. In the third step, we equilibrate the sample by allowing the particles to move for a period of time equal to $6\times10^3 T_0$. During equilibration, the stressed labile bonds are broken and new bonds are formed between the adjacent PGNs according to eq. (5). The equilibration process was monitored through the evolution of the average number of labile bonds and the sample length. We observed that the equilibration was essentially complete after the first $10^3 T_0$ of the equilibration time. During the remainder of equilibration step, the number of labile bonds and sample length changed by less than 1%. In the equilibrated sample, the PGNs formed a hexagonal lattice (as observed in recent experimental studies on a comparable system [13]). This hexagonal lattice is a stable configuration and alternative initial configurations of square and face centered square lattices spontaneously transformed to the hexagonal lattice during equilibration. In the fourth step, we establish the permanent bonds with the probability P. In this step, if two particles are linked with N_b bonds, then with the probability P, one of the bonds is designated as "permanent", so that the two particles become linked with ($N_b - 1$) labile bonds and one permanent bond. In this fifth step, the resultant sample composed of a dual-network of permanent and labile bonds is equilibrated for $10^4 T_0$ and then subject to tensile deformation by stretching at a constant velocity of 3.55 nm/s. The latter value of velocity is similar to that used in single molecule pulling experiments.[30]

The model parameters used in the simulations are listed in Table 1. For example, we considered a particle of core radius $r_0 = 50$ nm with $f = 156$ polymer chains grafted onto its surface such that the corona of grafted arms is of thickness $H = qr_0$. The value of f is used to determine the strength of repulsion (see eq. (1)) and the extent of bond formation between any two interacting particles through $N_{max}(R)$ (see eq.(5)). In eq.(2), we set $A = 1.15\sigma$, $B = 0.08\sigma$, and $C = 60k_BT$; at these values, the equilibrium distance between an isolated pair of PGNs without interconnecting bonds corresponds to $\sim 1\%$ corona overlap. (The overlap increases in the presence of bonds between the polymer arms.)

Place Table 1 here.

We examined labile bond energies, $U_0^{(l)}$ that varied from 33 to 39 k_BT and set the permanent bond energies, $U_0^{(p)}$, to 45 k_BT. These bond energies lie in the range relevant to disulfide bonds,[30-35] which can undergo exchange and "shuffling" reactions that enable the material to exhibit substantial structural rearrangements,[36,37] which in turn can impart self-healing behavior in polymer networks.[38-40] In the final example, we considered the effect of adding high-strength bonds (corresponding to bond energies of 100 k_BT) to the dual cross-linked network, and in this manner, designed materials that exhibit remarkable resistance to deformation.

2.3. Bond rupture between an isolated pair of particles

The response of the dual cross-linked PGN networks to mechanical deformations and the ultimate properties of the networks (e.g., strain at break and toughness) depend on the dynamics of breaking the strained inter-particle bonds. By considering the behavior of an isolated pair of interconnected PGNs, we can obtain valuable insight into the effect of various structural or dynamical features on the bond breakage and hence, the mechanical behavior of the samples. To this end, we considered the rates of rupture for a single bond, $-dp/dt$, as function of strain ε calculated according to eq. (6) for a system of two PGNs, which are pulled apart with a constant velocity. Here, the strain ε is calculated as the ratio of the change in the center-to-center distance between the particles to the equilibrium particle separation. Figure 2 shows the rates of rupture for the weaker labile ($U_0^{(l)} = 33k_BT$, red line), stronger labile ($U_0^{(l)} = 39k_BT$, blue line) and the permanent ($U_0^{(p)} = 45k_BT$, black lines) bonds. Specifically, Fig. 2a shows the rupture rates at the corona thicknesses of $q = 0.75$ and 1.25

and the velocity of $v = 0.001v_0$. As can be seen, the corona thickness (chain length) has very little effect on the rate of rupture for the weaker labile bonds, whereas the stronger labile bonds and permanent bonds break at a notably larger strain within the thicker corona. Figure 2b shows the rate of rupturing a single bond as two PGNs are pulled apart at two different velocities and the corona thickness of $q = 0.75$. The dashed and solid lines in Fig 2b correspond to the velocities of $v = 0.001$ and $0.005v_0$, respectively, and show that the bonds rupture at larger strains as the velocity of pulling increases.

Place Figure 2 here.

We also compared the rupture behavior of labile ($U_0^{(l)} = 37k_BT$), permanent ($U_0^{(p)} = 45k_BT$), and high-strength ($100k_BT$) bonds by focusing on a single pair of particles, which have the corona of thickness $q = 0.75$ and are pulled apart at a constant velocity of $v = 0.001v_0$. First, we used eq. (6) to obtain the bond rupture rate, $-(dp/dt)$, as a function of strain, ε, for a single bond of these different types (Fig 3a). Notably, the high-strength bonds rupture only at strains that are significantly higher and distributed within a narrower range of ε than the strains at break for the labile and permanent bonds. Then, using the simulation approach described above, we determined the normalized total force as a function of strain for a pair of particles that are initially connected by all three bond types and placed at the equilibrium separation distance. As shown in Fig. 3b, small strains are sufficient to rupture multiple labile bonds, with the last labile bond failing at $\varepsilon = 0.84$. The permanent bond survives up to a much higher strain of $\varepsilon = 1.95$. Finally, the high-strength bond ruptures at a large strain of $\varepsilon = 3.86$. Figures 3a and 3b demonstrate that the strains at break obtained in the simulations (Fig. 3b) are similar to the single bond predictions obtained by solving eq. (6). Moreover, given that $-(dp/dt)$ for the high-strength bond is negligibly small at the strains leading to the rupture of labile and permanent bonds, it is a reasonable to treat the high-strength bonds as unbreakable in our simulations. The latter simplifying assumption is used to obtain the results discussed further below.

Place Figure 3 here.

3. Ductility and toughness of dual cross-linked PGNs

Using the simulations described above, we analyzed the material's response to a tensile deformation, where the sample is stretched at a constant velocity (strain-controlled deformation). [2,4] In particular, we determined the resulting force, F, on the sample and the number of bonds per particle as a function of the strain, ε. The strain ε is calculated as the ratio of the extension of the sample to the original length. The velocity at which the sample is stretched is similar to the values used in single molecule pulling experiments.[30] The ductility of the sample is characterized by the strain at break, ε_b, which is determined as the strain where the force required for deformation exhibits a sharp drop, indicating that the sample has fractured into separate sections. The work done by the external force to fracture the sample (work-to-break) is a measure of the toughness of the material. We defined toughness, W, as the work-to-break per particle. W is determined by integrating the force-extension curve, and dividing the resulting work by the number of nanoparticles in the sample, N_{PGN}.

The behavior of the dual cross-linked PGNs was found to be highly dependent on the strength of the labile bonds and the fraction of permanent bonds within the network. The energies of the labile bonds were chosen so that for the weaker labile bonds ($U_0^{(l)} = 33\,k_BT$), the bond rupture rate is of the same order of magnitude as the tensile deformation strain rate, whereas for the stronger labile bonds ($U_0^{(l)} = 39\,k_BT$), the rupture rate is approximately two orders of magnitude lower than the strain rate. As described in the previous section, for $0 < P \leq 1$, the inter-particle links encompass a single permanent bond in addition to the existing labile bonds. The energy of the permanent bond was taken to be $U_0^{(p)} = 45\,k_BT$, which corresponds to a bond rupture rate that is approximately five orders of magnitude lower than the strain rate.

We first examined the material properties of dual cross-linked PGNs that have a corona thickness of $q = 0.75$ and are subjected to a strain-controlled tensile deformation applied at a constant velocity of $v = 1.0 \times 10^{-3}$ (corresponding to roughly 3.55 nm/s). Figures 4a and 4b show the respective force-strain curves for the samples having the weaker ($U_0^{(l)} = 33 k_B T$) and stronger ($U_0^{(l)} = 39 k_B T$) labile bonds at the fractions of permanent bonds of $P =$ 0, 0.6, and 1. Each curve corresponds to a single run of the simulations. The arrows pointing downwards indicate sample breakage.

Place Figure 4 here.

Figures 4a and 4b indicate that the behavior of the dual cross-linked PGNs under tensile deformation is similar to that of ductile polymeric materials.[41,42] Namely, at the smaller strains, dual cross-linked PGNs behave as elastic materials. At a strain of about 15-20%, the samples reach a yield point, after which the force F decreases. (Recall that this force represents the resistance of the material to deformation.) After the yield point, the material exhibits two distinct behaviors, which depend quite markedly on P. Specifically, the force can reach a local minimum and then increases before the breakage, as seen in at Fig 4a at $P =$ 0.6 and 1 and in Fig 4b at $P =$ 1. The latter force-strain behavior is characteristic of polymeric materials that exhibit cold-drawing and necking.[41,42] Alternatively, the force can continue to decrease until the sample breaks, as seen in Fig. 4a at P = 0 and Fig. 4b at $P =$ 0 and 0.6.

Figures 4a and 4b also reveal the significant effect that the energy of labile bonds has on the mechanical performance of dual cross-linked PGNs. The weaker labile bonds cannot withstand deformation without the presence of permanent bonds; namely, the force F varies around some low value at $P = 0$ (Fig. 4a). The sample becomes elastic only after a sufficient amount of permanent bonds is added, so that at $P=1$, the yield strain and force are about 15% and $10F_0$, respectively. In contrast, the sample having the stronger labile bonds with $P=0$ exhibits the yield point at 20% strain, and the force at yield is of $F \approx 38F_0$ (Fig 4b). Introducing the permanent cross-links to the PGNs linked by the stronger labile bonds increases the yield force up to $F \approx 50F_0$ at $P=1$, and modifies the post-yield behavior so that the sample exhibits quite pronounced cold-drawing/necking at $P=1$ (Fig 4b).

From plots such as those in Fig 4, we obtained the results in Fig 5 that show the strain at break ε_b (Fig. 5a) and toughness W (Fig 5b) of the samples, which contain the weaker (curves 1) and stronger (curves 2) labile bonds, as functions of the fraction of permanent bonds P. The data points and error bars shown in Fig 5 were obtained by averaging over eight independent simulation runs. By contrasting curves 1 and 2 in the plots in Fig. 5, it is clear that the presence of the permanent cross-links is crucial for improving mechanical performance if the labile bonds are weak. At lower fractions of permanent bonds, the PGNs having the weaker labile bonds exhibit a strain at break of about 0.25 (curve 1 in Fig. 5a at $P<0.2$) and very low toughness (curve 1 in Fig. 5b at $0<P\leq 0.4$). At higher values of P, the permanent bonds form an elastic skeleton in the latter system that leads to a notable improvement in the material properties. Namely, ductility of the system having the weaker labile bonds increases to $\varepsilon_b \approx 1.0$ at $P \geq 0.5$, and toughness of the system exhibits an increase from $W \approx 1F_0r_0$ at $P=0.5$ to $W \approx 3.5F_0r_0$ at $P=1$.

Place Figure 5 here.

In contrast, the PGNs linked with the stronger labile bonds produce a ductile, tough material even in the absence of the permanent bonds, i.e., at $P=0$ (see curves 2 in Fig. 5). The introduction of permanent bonds into the system does not affect the strain at break, which remains at $\varepsilon_b \approx 1.0$ for $0 \le P \le 1$. The permanent bonds, however, do improve the toughness of the material; namely, $W \approx 7F_0 r_0$ at $P = 0$ is increased to $W \approx 11F_0 r_0$ at $P = 1$.

It is noteworthy that at $P = 1$, the toughness of the sample with the stronger labile bonds is three times greater than that of the sample with the weaker labile bonds (Fig 5b), whereas the strain at break is the same in the two systems (Fig 5a). This behavior, as well as the overall effect of dual cross-linking on the mechanical properties of PGNs, can be better understood from the more detailed analyses we performed on the materials' tensile behavior, as discussed below.

In the course of sample deformation, the rupture of stressed labile bonds takes place simultaneously with the formation of new bonds within the overlapped coronas. Figures 6a and 6b show the respective numbers of labile bonds per particle in the systems having the weaker and stronger labile bonds as functions of the strain ε. Initially, $N_b^{(l)}$ drops upon the tensile deformation of a sample. Then, after the sample yields, the number of bonds exhibits an increase; the latter behavior is especially noticeable in the system having the stronger labile bonds (Fig 6b). The increase in $N_b^{(l)}$ indicates that the material is capable of self-healing, particularly in the sample with the stronger labile bonds.

Place Figure 6 here.

Figures 6a and 6b show that the number of labile bonds in the dual cross-linked PGNs is quite large. Specifically, at a strain of 50% and $P = 1$, there are about 11 labile bonds per one particle in the case of weaker bonds (Fig 6a), and about 20 labile bonds/particle in the case of stronger bonds (Fig 6b). Besides the labile bonds, all the PGNs are linked by the permanent bonds at $P = 1$. Figure 6c reveals that the relative contributions of the labile and permanent bonds to the force F are different and depend on the strength of labile bonds. In Fig 6c, the force-strain curves for the dual cross-linked PGNs at $P = 1$ are plotted together with a curve for a system labeled “permanent only” where the links between particles are comprised solely of a single permanent bond. The latter system was prepared using the same procedure as describe above, but the formation of the labile bonds was prohibited both initially and in the course of deformation.

It is evident from Fig 6c that the weaker labile bonds do not contribute to the force as curve 1 and the “permanent only” plots effectively coincide. On the other hand, the contribution of the stronger labile bonds to F is quite remarkable (as can be seen by comparing the blue line with the red and black lines in Fig. 6c). Not all the stronger labile bonds, however, contribute to the force. The latter observation follows from Fig 6d, which shows the same force-strain curves as in Fig 6c but after normalization by the total number of bonds in the system, F / N_b. As can be seen in Fig 6d, the force per one bond is lower in the dual cross-linked systems than that in the system containing only the permanent bonds.

Figures 6c and 6d indicate that the strain at break is controlled mostly by the permanent bonds. Indeed, after averaging over 8 runs, the values of ε_b for the systems shown in Fig. 6c and 6d were essentially equal. Namely, $\varepsilon_b = 0.95 \pm 0.04$ in the case of permanent bonds only, and $\varepsilon_b = 1.07 \pm 0.06$ and 1.0 ± 0.08 in the respective cases of weaker and stronger labile bonds at $P = 1$. These observations help explain the $P = 1$ curves in Fig. 5a, which show that the strain at break is approximately the same in the two systems involving labile bonds.

We obtained further physical insight into the data in Fig 6 by examining snapshots from simulations of the materials undergoing tensile deformation. Figure 7 shows samples containing the weaker (Fig. 7a) and stronger labile (Fig. 7b) bonds at $P = 1$ for strains of $\varepsilon =$ 0.95. These snapshots show just the particles and the labile bonds; for clarity, the permanent bonds are not displayed. The number of labile bonds in a link is indicated by the color code in Fig 7c.

Place Figure 7 here.

Figure 7 reveals that the weaker labile bonds break easily in the direction of the tensile deformation; as can be seen, there are only a few horizontal links in Fig 7a. This tensile deformation is accompanied by the contraction of the sample in the transverse direction. As a result, the newly formed labile bonds are normal to the direction of stretching, so they do not contribute to the tensile force. At $\varepsilon = 0.95$, the surviving weaker labile bonds form the prominent vertical "stripes".

The total number and distribution of stronger labile bonds in Fig 7b are quite different from the picture seen in Fig 7a. Specifically, Fig. 7b reveals that there are still many labile bonds along the stretching direction at $\varepsilon = 0.95$ and the network is still dense relative to that formed by the weaker labile bonds (Fig. 7a). The bonds seen in Fig. 7b give rise to the large tensile forces observed in Fig. 6c for $U_0^{(l)} = 39\,k_B T$.

Finally, we note that samples having the weaker and stronger labile bonds exhibit different modes of failure. In the case of the weaker bonds, the sample fractures perpendicular to the direction of stretching (not shown). The sample having the stronger labile bonds breaks due to the formation and growth of a void, as indicated by the arrows in Fig. 7b.

4. Improving tensile properties through addition of high-strength bonds

Building on the above studies, we introduced a third type of bonding interaction into the dual cross-linked PGN networks in an attempt to enhance the materials' resistance to significant mechanical deformation. Specifically, we introduced a fraction of high-strength interconnections between the nanoparticles, modeling polymer arms that are bound by bond energies of $100\,k_B T$, which is comparable to a carbon-carbon bond. As discussed in Section 2.3, in our simulations, these high-strength bonds can be assumed to be unbreakable. By focusing on the structural rearrangements within the material, we found that the addition of just a small fraction of these unbreakable bonds can lead to a new mode of failure, which then led to dramatically improved mechanical properties and provided a powerful means of mitigating the effects of damage.

In these simulations, we assigned the probability of an unbreakable chain between two bonded particles to be P_n, with at most one unbreakable chain per pair. We varied this probability in the range $0 \le P_n \le 0.3$, aiming is to keep P_n sufficiently low that the randomly placed unbreakable bonds did not form a percolating network in the system. To distinguish between the different strong bonds in the networks, in this section we use P_p to describe the probability of a permanent bond ($U_0^{(p)} = 45 k_B T$) between nanoparticles (originally defined as P in the previous section). Figures 8a and 8b show the strain at break and toughness for a series of samples with unbreakable chains. Here, we specify the quantity, P_t, which represents the sum of P_p and P_n. The red curve in Fig. 8 characterizes samples where $P_p = 1$ and P_n is varied in the range specified above; hence, in these samples, $1 \le P_t \le 1.3$. For comparison, we also display a series of samples where P_t varies in the same range, but here the system encompasses just permanent bonds with $1 \le P_p \le 1.3$ and no unbreakable bonds (blue curve).

Place Figure 8 here.

The data for samples lacking the unbreakable chains ($P_n = 0$) show that the strain at break remained approximately constant for increasing P_p (see Fig. 8a). There was, however, a slight increase in toughness with increases in P_p (see Fig. 8b).

In contrast, the samples encompassing the unbreakable chains (with $P_p = 1$) display a systematic increase for both ε_b and W with increases in P_n. The standard deviations around the average values, however, became progressively larger for larger values of P_n as seen in

Fig 8; thus, a significant improvement in mechanical properties was only achieved for $P_n \geq 0.25$. Notably, for samples with the largest fraction of unbreakable chains ($P_n = 0.3$), the average values of ε_b and W showed a two-fold increase relative to an equivalent system without unbreakable connections ($P_p = 1.3$ and $P_n = 0$).

To understand the origin of the large standard deviations in the above red curves, we determined the histograms shown in Fig. 9a for the strain at break and in Fig. 9b for the toughness. The plots showcase the effect of adding unbreakable chains at $P_n = 0.15$ by displaying three sets of data: the base case $P_p = 1$, $P_n = 0$ (the green bars), an increased number of permanent bonds $P_p = 1.15$, $P_n = 0$ (the blue bars), along with an equivalent set with unbreakable chains $P_p = 1$, $P_n = 0.15$ (the red bars). By comparing the green and blue bars, it is clear that the additional permanent bonds produce no difference in ε_b and only a marginal improvement to W; the distribution profiles for both measurements are similar in width and shape. On the other hand, the introduction of unbreakable chains has a large impact, considerably widening the distribution for both ε_b and W. In fact, the inclusion of unbreakable bonds produces some samples that are able to survive strains far in excess of any networks without such bonds. In addition, there is a clear reduction in samples that break at small strain.

Place Figure 9 here.

To gain further insight into the failure behavior, we examined snapshots of several networks. Figure 10 displays a series of snapshots at $\varepsilon = 0.45$, $\varepsilon = 0.90$, $\varepsilon = 1.35$, and $\varepsilon = 1.80$ for a network encompassing unbreakable chains that survives to a relatively large strain. At low strain, $\varepsilon = 0.45$, the network is still reasonably intact; by the next level of strain, $\varepsilon = 0.90$, several voids have formed within the structure. At further strain, $\varepsilon = 1.35$, the region labeled “A” has been severed, but the network remains connected via a single thread. Finally, the sample ruptures at $\varepsilon = 1.80$ with the label "B" pinpointing the bond that fails; by this point, the single thread that contains predominantly unbreakable links has grown in terms of length and the number of critical particles involved in the bridge. The formation of such thin filaments enables the network to potentially withstand high strain; this is a distinctive mode of failure and is not observed in networks without unbreakable chains. It is important to note that for larger sample sizes, the system will contain not just one long-lived interconnecting strand, but many such threads. The combined effect of these multiple strands would dramatically extend the value of ε_b relative to materials that do not contain the unbreakable bonds.

Place Figure 10 here.

5. Strain recovery and self-healing in dual cross-linked PGN networks

Having examined factors that affect the response of the cross-linked PGNs to an applied force, we then utilized our computer simulations to investigate how a deformed material recovered when this applied force was removed. These studies involved a three-step process that is similar to the comparable experimental procedures.[43,44] In the first step, the network was subjected to a strain-controlled tensile deformation by pulling the left edge of the sample at a constant velocity of $v = 1 \times 10^{-3} v_0$ until the desired maximal value of strain, $\varepsilon_{\max}$, was reached. The values of $\varepsilon_{\max}$ were chosen to be below anticipated values for the strain at break to ensure the sample remains intact. The external tensile force F acting on the left edge of the sample was recorded as a function of ε during the first step. In the second step, the force F was relaxed to zero at a constant rate over the period of time $10^4 T_0$, and the strain ε was recorded (force-controlled strain relaxation). The inelastic component of the deformation was characterized by the residual strain, ε_0, defined as the value of strain at the moment of time when $F = 0$. Finally, in the third step, the relaxation of the residual strain at zero external force was tracked over some period of time. To elucidate the mechanism of strain recovery, the samples were subjected to either a single or multiple cycles of the stretching and relaxation procedure.

Via the above procedure, we determined how the key parameters of the system affect the strain recovery and self-healing in networks that are subjected to this type of tensile loading and unloading. We first describe our findings on the effect of varying the energy of the labile bonds, $U_0^{(l)}$ in systems where the initial value of the average number of permanent bonds between a pair of neighboring PGNs was set equal to $P = 1$.

5.1. Effect of varying the bond energy of the labile bonds

To gain an understanding of how the bond energy of our labile bonds influences the strain recovery process, we considered the deformation of samples with $U_0^{(l)}$ = 33, 37, and $39\, k_B T$. As indicated in Fig. 11a, at $0 \le t \le 2.5 \times 10^4 T_0$, the samples were stretched at a constant strain rate until the strain reaches the maximal value of $\varepsilon_{\max} = 0.53$. Then, at $t > 2.5 \times 10^4 T_0$, the force F was released at a constant rate such that $F = 0$ at $t = 3.5 \times 10^4 T_0$. We use the term “recovery” for the relaxation processes that occur after $F = 0$ is reached. From these simulations, we obtained the set of plots in Fig. 11, which shows the strain ε (Fig. 11a) and number of labile bonds per particle $N_b^{(l)} / N_{PGN}$ (Fig. 11b) as a function of time t.

Place Figure 11 here.

Figure 11 clearly shows that the behavior of the dual cross-linked PGNs depends strongly on the strength of the labile bonds. In particular, Fig. 11a indicates that some part of this deformation is inelastic since the samples exhibit residual strain upon release of the external load; the residual strain is considerably lower in the sample having the weaker labile bonds than in the other two samples (compare curve 1 with curves 2 and 3 in Fig. 11a). Additionally, Fig. 11a shows that the recovery of the residual strain in the unloaded samples at $t > 3.5\times10^4 T_0$ becomes slower as the energy of labile bonds increases from $U_0^{(l)} = 33k_B T$ (curve 1) to 37 and $39k_B T$ (curves 2 and 3, respectively).

During the course of the deformation, the rupture of stressed labile bonds occurs simultaneously with the formation of new bonds within the overlapped coronas. Figure 11b shows that $N_b^{(l)} / N_{PGN}$ drops during the initial stretching of a sample, and this decrease slows down even though the stretching continues. The latter behavior indicates that the rupture of stressed bonds is balanced by bond formation. Further, Fig. 11b shows that owing to the bond formation, the labile bonds are restored in the samples during the release of force ($N_b^{(l)} / N_{PGN}$ increases at $2.5\times10^4 T_0 < t < 3.5\times10^4 T_0$), thus, clearly indicating that the material is capable of self-healing. Figure 11b indicates that during the strain controlled stretching there is greater number of the labile bonds in the samples with higher $U_0^{(l)}$.

The relaxation of strain and of the labile bonds continues in the system after the tensile force is released and the system reaches the $F = 0$ state. To highlight this behavior, we specifically focused on the time frame around $F = 0$ in Figs. 11c and 11d, where $\Delta t = 0$ corresponds to $t = 2.5\times10^4 T_0$, the beginning of the controlled release of the force on the stretched sample. Note that Figs. 11c and 11d show the behavior of the system during the release of force and recovery ($t > 2.5\times10^4 T_0$), as well as the dynamics of recovery at longer times (up to $5\times10^5 T_0$). From the latter plots, we clearly see that the rate and extent of recovery depend on the energy of the labile bonds. In the system having the weaker labile bonds ($U_0^{(l)} = 33k_B T$), the recovery occurs during $\sim 1\times10^4 T_0$ (see Fig. 11c). The residual strain, however, is not completely recovered and remains about 4% in this case. Additionally, the number of labile bonds is lower than its initial value (as can be seen by comparing curve 1 at $t = 0$ in Fig. 11b and late times in Fig. 11d). In contrast, at the labile bond energies of $U_0^{(l)} = 37$ and $39 k_B T$, the recovery is markedly slower than in the case of weaker bonds and takes about $1 \times 10^5 T_0$ and $5 \times 10^5 T_0$, respectively (see Fig. 11c). Furthermore, in these cases, the strain and the number of labile bonds exhibit a complete recovery that occurs in two distinct stages, as can be seen from curves 2 and 3 in Figs. 11c and 11d, respectively. At the first stage, the number of labile bonds relax close to the value before the deformation, while in the second stage, strain recovery happens around a constant value of $N_b^{(l)} / N_{PGN}$.

Recovery of the residual strain and the labile bonds at $F = 0$ and beyond occurs through local rearrangements of the PGNs. The motion of these nanoparticles relative to each other is limited by the rate of breakage of the labile bonds. Note that the labile bonds break less often as the bond energy is increased. Therefore, the rate of recovery decreases with an increase in $U_0^{(l)}$. It is worth recalling that $U_0^{(l)}$ also controls the degradation of the cross-linked system in the course of deformation, as discussed in Section 3. An increase in the energy of labile bonds from 33 to $37 k_B T$ and higher, prevents the formation of large voids, which cannot be healed during recovery. Hence, complete strain recovery is observed at $U_0^{(l)} = 37$ and $39 k_B T$.

5.2. Role of permanent bonds in strain recovery

Permanent bonds form an elastic skeleton in the dual cross-linked nanoparticle network; the presence of these bonds can lead to notable improvements in the toughness of the material as shown in Section 3. We found that the permanent bonds between the PGNs also play an important role in the strain recovery within the sample. Specifically, we varied the average number of permanent bonds between two particles over the range $1 \le P \le 2$, while fixing the labile bond energy at $U_0^{(l)} = 37k_B T$, and applied a strain up to $\varepsilon_{\max} = 0.53$. We then monitored the behavior of the material during the force-controlled relaxation process (for $10^4 T_0$) and the subsequent the recovery period.

We can obtain insight into the effect of permanent bonds by examining snapshots from simulations of samples in the process of recovery, i.e., after the force in the sample is released ($\Delta t = 10^4 T_0$). Figures 12a,b and 12c,d show the nanoparticles and the labile bonds in the samples at $P = 1$ and $P = 2$, respectively, at $\Delta t = 1.5 \times 10^4 T_0$ and $7.5 \times 10^4 T_0$, where $\Delta t = 10^4 T_0$ corresponds to the moment of time when the force is totally released and the recovery begins. Figures 12a and 12b reveal that for $P = 1$, there are a number of voids of various sizes distributed throughout the sample during recovery. In contrast, Figures 12c and 12d show that upon unloading all the voids are healed by $\Delta t = 7.5 \times 10^4 T_0$ due to the increase in the number of permanent bonds from $P = 1$ to $P = 2$.

Place Figure 12 here.

5.3. Strain recovery under cyclic stretching and relaxation

In the previous section, we showed that the extent of healing after a single strain and relaxation cycle depends on the fraction of the permanent bonds in the network. We also examined the recovery process for systems subjected to multiple cycles of strain and relaxation. We quantified the influence of P on the properties of materials undergoing multiple deformations by calculating the hysteresis ΔW, which is defined as the area confined within a force-strain loop. Figure 13 shows the material properties of samples that are subjected to repeated deformations where the maximal strain, $\varepsilon_{\max}$, is increased incrementally with each subsequent cycle. Namely, $\varepsilon_{\max} = 0.1$ in the first cycle and $\varepsilon_{\max} = 0.53$ in the fifth cycle. As above, the consecutive cycles of strain-controlled tensile deformation are followed by the force-controlled relaxation during $10^4 T_0$ and the samples can recover for

$5 \times 10^4 T_0$ before the next cycle. Figures 13a and 13b show the respective force-strain curves for five consecutive cycles in systems with fractions of permanent bonds equal to $P = 1$ and $P =$ 2. Each curve corresponds to a single simulation run at $U_0^{(l)} = 37 k_B T$. While the residual strain increases with each increase in $\varepsilon_{\max}$, the healing of both of the samples is complete for $\varepsilon_{\max} < 0.42$; that is, the strain eventually goes back to $\varepsilon = 0$. Above that value of strain, however, the recovery is incomplete in the $P = 1$ sample (see Fig. 13a). Notably, the sample involving $P = 2$ recovers completely after each cycle (Figure 13b).

Place Figure 13 here.

Figure 13c shows that the hysteresis ΔW increases with an increase in the maximal strain for all samples at $\varepsilon_{\max} < 0.42$. Furthermore, while the hysteresis of the samples at $P = 2$ is slightly lower than that at $P = 1$ at $\varepsilon_{\max} < 0.42$ and continues to increase for increasing strains, the hysteresis for the $P = 1$ samples levels off at $\varepsilon_{\max} > 0.31$. The results indicate that there is greater energy loss with increasing maximum strain, in particular, due to the increase in the residual strain. In addition, at $\varepsilon_{\max} \le 0.31$, the energy loss is greater at $P = 1$ than that at $P = 2$. For greater strains, the deterioration of the sample that occurs at $P = 1$ leads to a reduction in ΔW (see Fig. 13a and curve 1 in Fig. 13c). Thus, an increase in the fraction of permanent bonds provides a clear improvement in the self-healing ability of the PGN network, enabling enhanced recovery from mechanical damage even after multiple cycles of deformation.

6. Conclusions

The cross-linked PGN networks considered here have the potential for exhibiting a remarkable combination of flexibility, strength and toughness. In order to optimize the performance of these advantageous composites, we formulated a hybrid model that integrates the hierarchy of structural features and temporal events that characterize the behavior of these materials. Namely, our model encompasses: 1) the structural details of each PGN, 2) the interaction between adjacent PGNs, 3) the kinetics of rupturing/forming individual bonds between the polymer arms on neighboring particles, and 4) the response of entire sample to mechanical deformation. Using this multi-scale model, we focused on systems of dual cross-linked PGNs that are interconnected by both strong "permanent" bonds and weaker labile bonds, and determined the response of the material to tensile deformation. To establish the critical parameters controlling the material's mechanical behavior, we varied the bond energies of the labile bonds, $U_0^{(l)}$, and the amount of permanent bonds P in the network. We also introduced a fraction of high-strength ("unbreakable") bonds, P_n , in the system and determined how variations in P_n affected the materials' tensile properties. In effect, these variables provided key parameters for tailoring the performance of the composites.

We found that the presence of permanent bonds plays a critical role primarily in the material encompassing the weaker labile bonds, $U_0^{(l)} = 33k_BT$. In these materials, increases in P led to significant improvements in the ductility and the toughness of the dual cross-linked network. In contrast, in the case of the stronger labile bonds, $U_0^{(l)} = 39k_BT$, the PGN network formed a ductile, tough material even at $P = 0$, and introduction of the permanent bonds primarily led to increases in the toughness. Notably, at $P = 1$, the toughness of the sample with the stronger labile bonds was three times greater than that of the sample with the weaker labile bonds. Furthermore, within a network connected by a $P = 1$ skeleton of permanent bonds, the mode of failure depended on the nature of the labile bonds. While the networks with the weaker labile bonds failed by rupturing in a direction perpendicular to the deformation, the network with the stronger labile bonds failed through the growth of cavities within the sample. These findings elucidate how the labile bond energies influence the performance of the entire cross-linked network.

It is noteworthy that at $P = 1$, the strain at break, ε_b, was controlled primarily by the permanent bonds in both of the materials containing the weaker and stronger labile bonds. Namely, for the both types of samples, it is ultimately the permanent bonds that bear the force from the deformation and ultimately, it is their rupture that determines the value of ε_b.

The above results indicate that the mechanical response of a dual cross-linked network can be controlled by modifying either the bond energies of the labile bonds or the fraction of permanent bonds in the network. Specifically, we showed that for a network with weaker labile bonds, an increase in fraction of permanent bonds can yield a tough network that behaves like a polymeric material, which exhibits cold drawing/necking. On the other hand, similar changes to the network with stronger labile bonds lead to an increase in toughness, with the network characteristics being similar to that of a purely ductile material.

We also found that the inclusion of a small amount of unbreakable chains has a dramatic effect on the response of the network to mechanical deformation. Notably, a distinct fraction of samples with unbreakable links could survive strains far greater than any networks with just labile and permanent bonds. This behavior is evident from histograms for the strain at break and toughness, which exhibited a significant broadening relative to comparable networks without unbreakable connections. The presence of unbreakable links can lead to the formation of long thin threads that can hold the entire network intact. The latter behavior is due to the ability of unbreakable chains to extend over large gaps and hold tremendous loads without rupturing. These findings provide valuable guidelines for creating materials that display remarkable ductility and strength.

Finally, we examined the strain recovery and healing behavior of the dual cross-linked PGN networks. Our findings showed that the residual strain within the material decreases with an increase in the energy of the labile bonds. The increase in $U_0^{(l)}$ did, however, also lead to an increase in the time needed for recovery; this is due to the resultant decrease in the rate of bond breakage and the concomitant slowing down of the particle rearrangements. These results highlight a competition between the extent and the rate of recovery with variations in the energy of labile bonds. For the systems considered here, we determined that the value of $U_0^{(l)} = 37k_BT$ led to an optimal compromise. Specifically, the latter samples displayed complete recovery, as opposed to the systems involving $U_0^{(l)} = 33k_BT$ bonds, and achieved this recovery in a shorter time than systems encompassing the $U_0^{(l)} = 39k_BT$ bonds.

By examining snapshots from the simulations, we found that during recovery networks containing the permanent bonds at $P = 2$ displayed a more pronounced closure of the voids within the samples and hence, greater healing than the $P = 1$ materials. We also examined how variations in the amount of permanent bonds in the system affect the extent of healing and recovery that occurs after the PGN networks were subjected to multiple cycles of stretching and relaxation. Using the hysteresis, ΔW, as a measure of the extent of damage recovery, we found that the $P = 1$ materials showed progressive deterioration with consecutive cycles of stretching and relaxation. In contrast, at a higher amount of permanent cross-links ($P = 2$), the networks recovered completely after consecutive cycles of stretching and relaxation.

In summary, the results of these computer simulations reveal how choices in the design space (e.g., energy of labile bonds and fraction of permanent and high-strength bonds) affect the final mechanical performance of the material. Such models allow researchers to understand how variations in key parameters can be harnessed to tailor the behavior of the material and thus, facilitate the fabrication of the next generation of nanocomposites with novel and technologically useful properties.

Acknowledgements

Research supported by the U.S. Department of Energy, Office of Basic Energy Sciences, Division of Materials Sciences and Engineering under Award DEFG-02-02ER45998 (A.C.B and K.M.), which was used to support BVSI and MJH (to perform the simulations). Financial support from the Army Research Office under Award W911NF-10-1-0486 (A.C.B) was used to support VVY (to perform the analytical studies).

References

[1] Yang W, Chen IH, Bernd G, Zimmerman EA, Ritchie RO, Meyers MA. Natural Flexible Dermal Armor. Adv Mater 2013;25:31-48.

[2] Iyer BVS, Salib IG, Yashin VV, Kowalewski T, Matyjaszewski K, Balazs AC. Modeling the response of dual cross-linked nanoparticle networks to mechanical deformation. Soft Matter 2013;9:109-121.

[3] Iyer BVS, Yashin VV, Kowalewski T, Matyjaszewski K, Balazs AC. Strain recovery and self-healing in dual cross-linked nanoparticle networks. Polym Chem 2013;4:4927-4939.

[4] Hamer MJ, Iyer BVS, Yashin VV, Kowalewski T, Matyjaszewski K, Balazs AC. Modeling polymer grafted nanoparticle networks reinforced by high-strength chains. Soft Matter 2014;10:1374-1383.

[5] Kim HK, Lee CH, Sudeep PK, Emrick T, Crosby AJ. Nanoparticle Stripes, Grids, and Ribbons Produced by Flow Coating. Adv Mater 2010;22:4600-4604.

[6] Lee DY, Pham JT, Lawrence J, Lee CH, Parkos C, Emrick T, Crosby AJ. Macroscopic Nanoparticle Ribbons and Fabrics. Adv Mater 2013;25:1248-1253.

[7] Mueggenburg KE, Lin XM, Goldsmith RH, Jaeger HM. Elastic membrane of close-packed nanoparticle arrays. Nat Mater 2007;6:656-660.

[8] Akcora P, Liu H, Kumar SK, Moll J, Li Y, Benicewicz BC, Schadler LS, Acehan D, Panagiotopoulos AZ, Pryamitsyn V, Ganesan V, Ilavsky J, Thiyagarajan P, Colby RH, Douglas JF. Anisotropic self-assembly of spherical polymer-grafted nanoparticles. Nat Mater 2009;8:354-359.

[9] Voudouris P, Choi J, Gomopoulos N, Sainidou R, Dong H, Matyjaszewski K, Bockstaller MR, Fytas G. Anisotropic Elasticity of Quasi-One-Component Polymer Nanocomposites. ACS Nano 2011;5:5746-5754.

[10] Agarwal P, Chopra M, Archer LA. Nanoparticle Netpoints for Shape-Memory Polymers. Angew Chem Int Ed 2011;50:8670-8673.

[11] Choi J, Hui CM, Pietrasik J, Dong H, Matyjaszewski K, Bockstaller MR. Toughening fragile matter: mechanical properties of particle solids assembled from polymer-grafted hybrid particles synthesized by ATRP. Soft Matter 2012;8:4072-4082.

[12] Fernandes NJ, Koerner H, Giannelis EP, Vaia RA. Hairy nanoparticle assemblies as one-component functional polymer nanocomposites: opportunities and challenges. MRS Commun 2013;3:13-29.

[13] Chen Y, Guan Z. Self-assembly of core-shell nanoparticles for self-healing materials. Polym Chem 2013;4:4885-4889.

[14] Kumar SK, Jouault N, Benicewicz B, Neely T. Nanocomposites with Polymer Grafted Nanoparticles. Macromolecules 2013;46:3199-3214.

[15] Choi J, Hui CM, Schmitt M, Pietrasik J, Margel S, Matyjaszewski K, Bockstaller MR. Effect of polymer-Graft Modification on the Order Formation in Particle Assembly Structures. Langmuir 2013;29:6452-6459.

[16] Gong JP, Katsuyama Y, Kurokawa T, Osada Y. Double-Network Hydrogels with Extremely High Mechanical Strength. Adv Mater 2003;15:1155-1158.

[17] Gong JP. Why are double network hydrogels so tough? Soft Matter 2010;6:2583-2590.

[18] Webber RE, Creton C, Brown HR, Gong JP. Large Strain Hysteresis and Mullins Effect of Tough Double-Network Hydrogels. Macromolecules 2007;40:2919-2927.

[19] Nakajima T, Kurokawa T, Ahmed S, Wu WL, Gong JP. Characterization of internal fracture process of double network hydrogels under uniaxial elongation. Soft Matter 2013;9:1955-1966.

[20] Likos CN, Löwen H, Watzlawek M, Abbas B, Jucknischke O, Allgaier J, Richter D. Star polymers viewed as ultrasoft colloidal particles. Phys Rev Lett 1998;80:4450-4453.

[21] Jusufi A, Watzlawek M, Löwen H. Effective Interaction between Star Polymers. Macromolecules 1999;32:4470-4473.

[22] Daoud M, Cotton JP. Star shaped polymers: a model for the conformation and its concentration dependence. J Phys (Paris) 1982;43:531-538.

[23] Lo Verso F, Likos CN, Reatto L. Star polymer with tunable attractions: cluster formation, phase separation, reentrant crystallization. Prog Colloid Polym Sci 2006;133:78-87.

[24] Dobrynin AV, Carrillo YJ. Universality in Nonlinear Elasticity of Biological and Polymeric Networks and Gels. Macromolecules 2011;44:40-146.

[25] Bell GI. Model for the specific adhesion of cells to cells. Science 1978;200:618-627.

[26] Bell GI, Dembo M, Bongrad P. Competition Between Nonspecific Repulsion and Specific Bonding. Biophys J 1984;45:1051-1064.

[27] Bhatia SK, King MR, Hammer DA. The State Diagram for Cell Adhesion Mediated by Two Receptors. Biophys J 2003;84:2671-2690.

[28] Diezemann G, Janshoff A. Dynamic force spectroscopy: Analysis of reversible bond-breaking dynamics. J Chem Phys 2008;129:084904/1-10.

[29] Wijmans CM, Zhulina EB. Polymer Brushes at Curved Surfaces. Macromolecules 1993;26:7214-7224.

[30] Wiita AP, Ainavarapu SRK, Huang HH, Fernandez JM. Force-dependent chemical kinetics of disulfide bond reduction observed with single-molecule techniques. PNAS 2006;103:7222-7227

[31] Dopieralski P, Ribas-Arino J, Anjukandi P, Krupicka M, Kiss J, Marx D. The Janus-faced role of external forces in machanochemical disulfide bond cleavage. Nat Chem 2013;5:685-691.

[32] Garcia-Manyes S, Liang J, Szoskiewicz R, Kuo TL. Fernandez JM, Force-activated reactivity switch in a bimolecular chemical reaction. Nat Chem 2009;1:236-242.

[33] Li Y, Nese A, Lebedeva NV, Davis T, Matyjaszewski K, Sheiko SS. Molecular Tensile Machines: Intrinsic Acceleration of Disulfide Reduction by Dithiothreitol. J Am Chem Soc 2011;133:17479-17484.

[34] Lebedeva NV, Nese A, Sun FC, Matyjaszewski K, Sheiko SS. Anti-Arrhenius cleavage of covalent bonds in bottlebrush macromolecules on substrate. PNAS 2012;109:9276-9280.

[35] Li Y, Nese A, Matyjaszewski K, Sheiko SS. Molecular Tensile Machines: Anti-Arrhenius Cleavage of Disulfide Bonds. Macromolecules 2013;46:7196-7201.

[36] Yoon JA, Kamada J, Koynov K, Mohin J, Nicolay R, Zhang YZ, Balazs AC, Kowalewski T, Matyjaszewski K. Self-Healing Polymer Films Based on Thiol-Disulfide Exchange Reactions and Self-Healing Kinetics Measured Using Atomic Force Microscopy. Macromolecules 2012;45:142-149.

[37] Amamoto Y, Otsuka H, Takahara A, Matyjaszewski K. Self-Healing of Covalently Cross-Linked Polymers by Reshuffling Thiuram Disulfide Moieties in Air under Visible Light. Adv Mater 2012;24:3975-3980.

[38] Kolmakov GV, Matyjaszewski K, Balazs AC. Harnessing Labile Bonds between Nanogel Particles to Create Self-Healing Materials. ACS Nano 2009;3:885-892.

[39] Salib IG, Kolmakov GV, Gnegy CN, Matyjaszewski K, Balazs AC. Role of Parallel Reformable Bonds in the Self-Healing of Cross-Linked Nanogel Particles. Langmuir 2011;27:3991-4003.

[40] Duki SF, Kolmakov GV, Yashin VV, Kowalewski T, Matyjaszewski K, Balazs AC. Modeling the nanoscratching of self-healing materials. J Chem Phys 2011;134:084901/1-12.

[41] Kinloch AJ, Young RJ. Fracture Behaviour of Polymers. London: Applied Science Publishers, 1983. 496 pp.

[42] Ward IM, Sweeney J. An Introduction to the Mechanical Properties of Solid Polymers. Chichester: John Wiley & Sons Inc, 2004. 382 pp.

[43] Zhang H, Scholz AK, Vion-Loisel F, Yannick M, Brieu M, Brown H, Roux S, Kramer EJ, Creton C. Opening and Closing of Nanocavities under Cyclic Loading in a Soft Nanocomposite Probed by Real-Time Small-Angle X-ray Scattering. Macromolecules 2013;46:900-913.

[44] Rose S, Dizeux A, Narita T, Hourdet D, Marcellan A. Time Dependence of Dissipative and Recovery Processes in Nanohybrid Hydrogels. Macromolecules 2013;46:4095-4104.

Figure captions

Fig. 1. Hierarchy of interactions in a network of dual cross-linked polymer grafted nanoparticles (PGNs). The grafted polymer chains contain reactive end groups, which interact to form labile, permanent, or unbreakable bonds and thus, the model captures phenomena on the scale of bond formation (and rupture). At the nanoscopic scale, each spherical nanoparticle is represented by a rigid core that encompasses a corona of grafted chains. The overlapping of the coronas on neighboring particles enables the formation of

multiple bonds between the nanoparticles. Finally, via the interactions between the PGNs and formation of bonds, the coated nanoparticles form an extended mesoscopic network.

Fig. 2. Effect of corona thickness, q, and pulling velocity, v, on bond rupture rate, $-dp/dt$, at bond energies $U_0^{(l)}/k_BT$=33, 39, and 45 (red, blue, and black curves, respectively). (a) Bond rupture rate ($-dp/dt$) versus strain (ε) curves for q=0.75 and 1.25 (dashed and solid lines, respectively). (b) Bond rupture rate ($-dp/dt$) versus strain (ε) curves for v=0.001 and 0.005 (dashed and solid lines, respectively).

Fig. 3. (a) Bond rupture rate, $-(dp/dt)$, as a function of strain, ε, for a single labile, permanent, and high-strength ($100k_BT$) bond, each with an initial equilibrium separation of $R_0 = 3.21$. Inset shows the plot for the high-strength bond in greater detail. (b) Force, F, versus strain, ε, from a constant strain rate pulling simulation for a pair of particles connected by multiple labile (red) bonds ($37k_BT$) along with a single permanent (gray) bond ($45k_BT$) and a high-strength (black) bond, beginning at an equilibrium separation of $R_0 = 3.15$. The downward arrow indicates complete rupture of all bonds.

Fig. 4. Effect of fraction of permanent bonds, P, on mechanical response of network. (a) Force(F) versus strain(ε) curves at P=0, 0.6, and 1 (black, green, and red curves, respectively) for $U_0^{(l)}/k_BT = 33$ (b) Force (F) versus strain (ε) curves at P=0, 0.6, and 1 for $U_0^{(l)}/k_BT = 39$.

Fig. 5. Effect of fraction of permanent bonds, P, and labile bond energy, $U_0^{(l)}/k_BT$, on strain at break, ε_b, and toughness, W, (red and blue lines denote $U_0^{(l)}/k_BT$=33 and 39,

respectively). (a) Strain at break, ε_b, as a function of fraction of permanent bonds, P. (b) Toughness, W, as a function of fraction of permanent bonds, P.

Fig. 6. Effect of labile bond energy, $U_0^{(l)}/k_BT$ (a) Number of labile bonds/particle, $N_b^{(l)}/N_{PGN}$, as a function of strain, ε, at P=0, 0.6, and 1 for $U_0^{(l)}/k_BT = 33$. (b) Number of labile bonds/particle, $N_b^{(l)}/N_{PGN}$, as a function of strain, ε, at P=0, 0.6, and 1 for $U_0^{(l)}/k_BT = 39$. (c) Force (F) versus strain (ε) curves for $U_0^{(l)}/k_BT$=33, 39, and in the absence of labile bonds (red, blue, and black curves, respectively). (d) Normalized force per bond, F/N_b, versus strain, ε, curves for $U_0^{(l)}/k_BT$=33, 39, and in the absence of labile bonds.

Fig. 7. (a) Snapshot of weaker labile bonds ($U_0^{(l)}/k_BT = 33$) sample with $P=1$ at strain ε = 0.95. (b) Snapshot of stronger labile bonds ($U_0^{(l)}/k_BT = 39$) sample with $P=1$ at strain ε = 0.95. (c) The color of the lines indicates the number of labile bonds in the link.

Fig. 8. (a) Strain at break, ε_b, and (b) toughness, W, as a function of the average number of extra bonds per neighboring pair in the range $1 \le P_t = P_p + P_n \le 1.3$. Networks with solely permanent bonds, ($1 \le P_p \le 1.3, P_n = 0$), are compared with networks that contain added unbreakable chains ($P_p = 1, 0 \le P_n \le 0.3$). The average values and standard deviations were obtained according to the Weibull statistics.

Fig. 9. Histograms of the (a) strain at break and (b) toughness for three different bond formation scenarios: the base case of permanent bonds with no unbreakable chains per pair ($P_p = 1, P_n = 0$), an increase in the average number of permanent bonds per pair ($P_p = 1.15, P_n = 0$), and an equivalent system with $P_t = 1.15$ composed of permanent bonds at

$P_p = 1$ and the unbreakable chains introduced at $P_n = 0.15$. The average value and standard deviation obtained according to the Weibull statistics are shown for each distribution. The average value and standard deviation obtained from Weibull statistics are shown by the respective points and error bars for each of the cases (green ($P_p = 1, P_n = 0$), blue ($P_p = 1.15, P_n = 0$) and red ($P_p = 1, P_n = 0.15$)).

Fig. 10. Snapshots of sample with $P_p = 1$, $P_n = 0.15$ at strains $\varepsilon = 0.45$, $\varepsilon = 0.90$, $\varepsilon = 1.35$, and $\varepsilon = 1.80$ (at the point of rupture). The thick gray and black lines indicate the permanent bonds and unbreakable chains, respectively. The cores with an unbreakable connection are colored red, and those without an unbreakable connection are colored blue.

Fig. 11: Effect of varying the labile bond energy, $U_0^{(l)}/k_B T$, on network response at $P = 1$. The network is subject to tensile stretching at a constant velocity followed by a controlled linear force release and recovery at zero-force. (a) Strain (ε) versus time (t) curves for $U_0^{(l)}/k_B T =$ 33, 37, and 39. (b) Number of labile bonds per particle ($N_b^{(l)}/N_{PGN}$) versus time(t) curves for $U_0^{(l)}/k_B T =$ 33, 37, and 39. (c) Strain (ε) versus time (Δt) curves, for $U_0^{(l)}/k_B T =$ 33, 37, and 39. (d) Number of labile bonds per particle ($N_b^{(l)}/N_{PGN}$) versus time(Δt) curves for $U_0^{(l)}/k_B T =$ 33, 37, and 39. Note in (c) and (d), the time $\Delta t = 0$ corresponds to $t = 2.5 \times 10^4 T_0$, the beginning of the controlled force release on the stretched sample.

Fig. 12: Snapshots of sample with $U_0^{(l)}/k_B T = 37$ during recovery at (a) $\Delta t = 1.5 \times 10^4 T_o$ and (b) $\Delta t = 7.5 \times 10^4 T_0$ with fraction of permanent bonds $P = 1.0$, (c) $\Delta t = 1.5 \times 10^4 T_o$ and (d) $\Delta t = 7.5 \times 10^4 T_0$ with fraction of permanent bonds $P = 2.0$.

Fig. 13: Effect of strain-relaxation cycles on the recovery of the samples as the maximum strain is increased to $\varepsilon_{\max}$ = 0.1, 0.2, 0.31, 0.42, and 0.53 in consecutive cycles. Here, $U_0^{(l)}/k_B T = 37$. (a) Force (F) versus strain (ε) curves for repeated cycles at $P = 1$. (b) Force (F) versus strain (ε) curves for repeated cycles at $P = 2$. (c) Hysteresis, ΔW, as a function of number of cycles at P =1 and 2. Open circles indicate conditions where one of the eight samples fractured during the course of being strained.

Fig. 1.

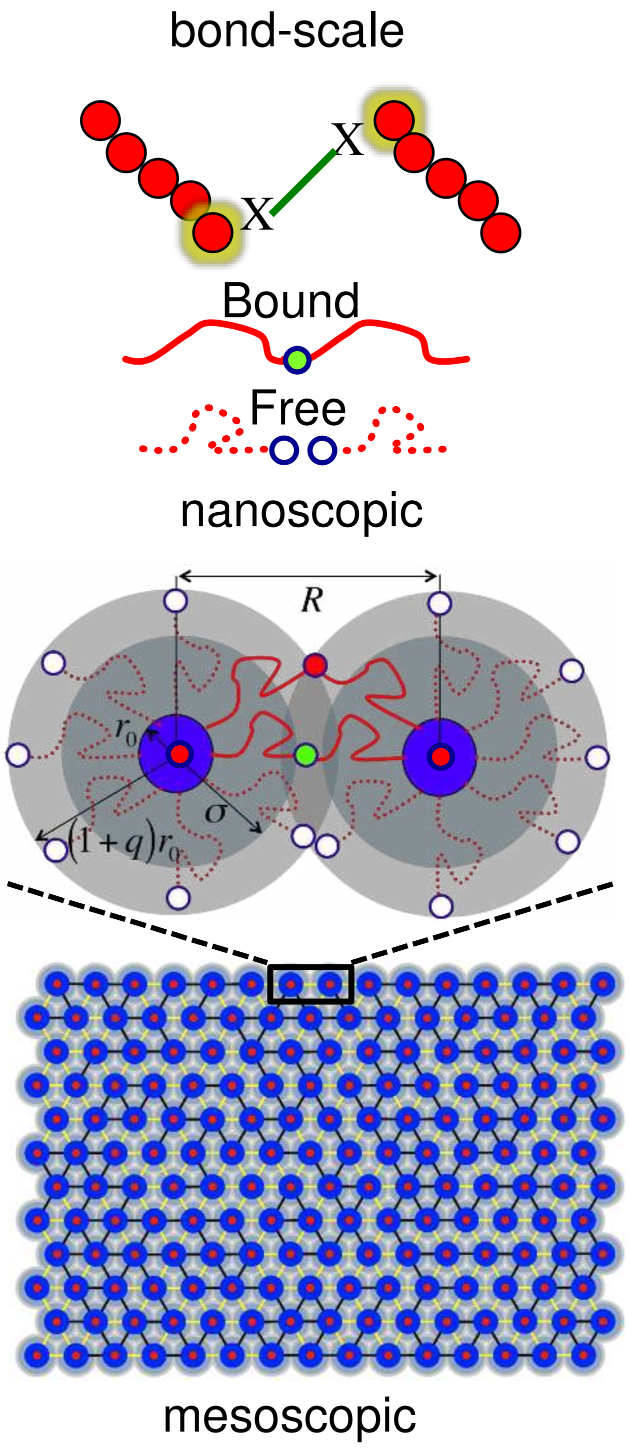
bond-scale
X
X
Bound
Free
nanoscopic
R
r_0
σ
$(1+q)r_0$
mesoscopic

Fig. 2.

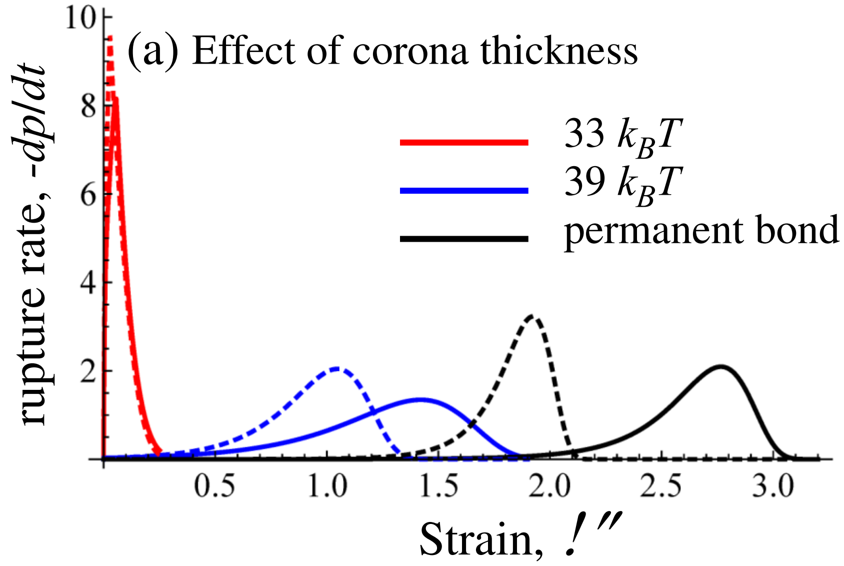
(a) Effect of corona thickness
33 k_BT
39 k_BT
permanent bond
rupture rate, -*dp*/*dt*
10
8
6
4
2
0.5
1.0
1.5
2.0
2.5
3.0
Strain, !″

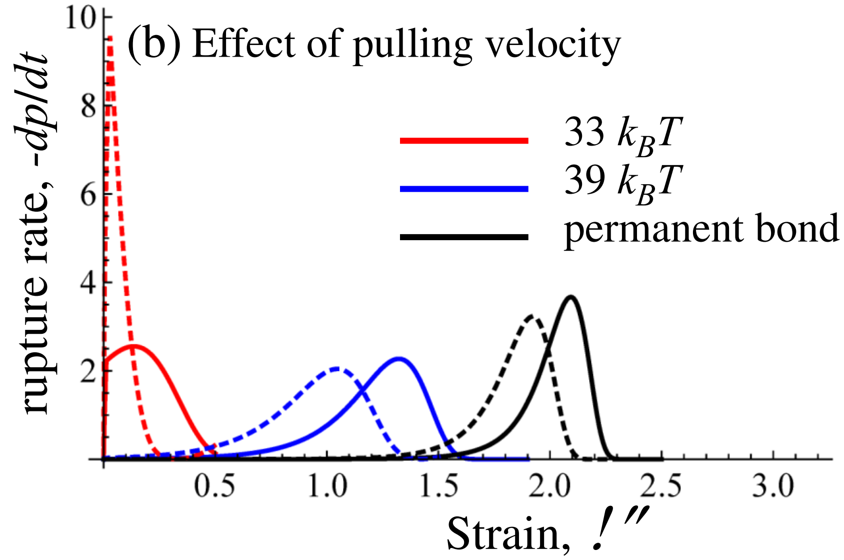
(b) Effect of pulling velocity
33 k_BT
39 k_BT
permanent bond
rupture rate, -*dp*/*dt*
10
8
6
4
2
0.5
1.0
1.5
2.0
2.5
3.0
Strain, !″

Fig. 3.

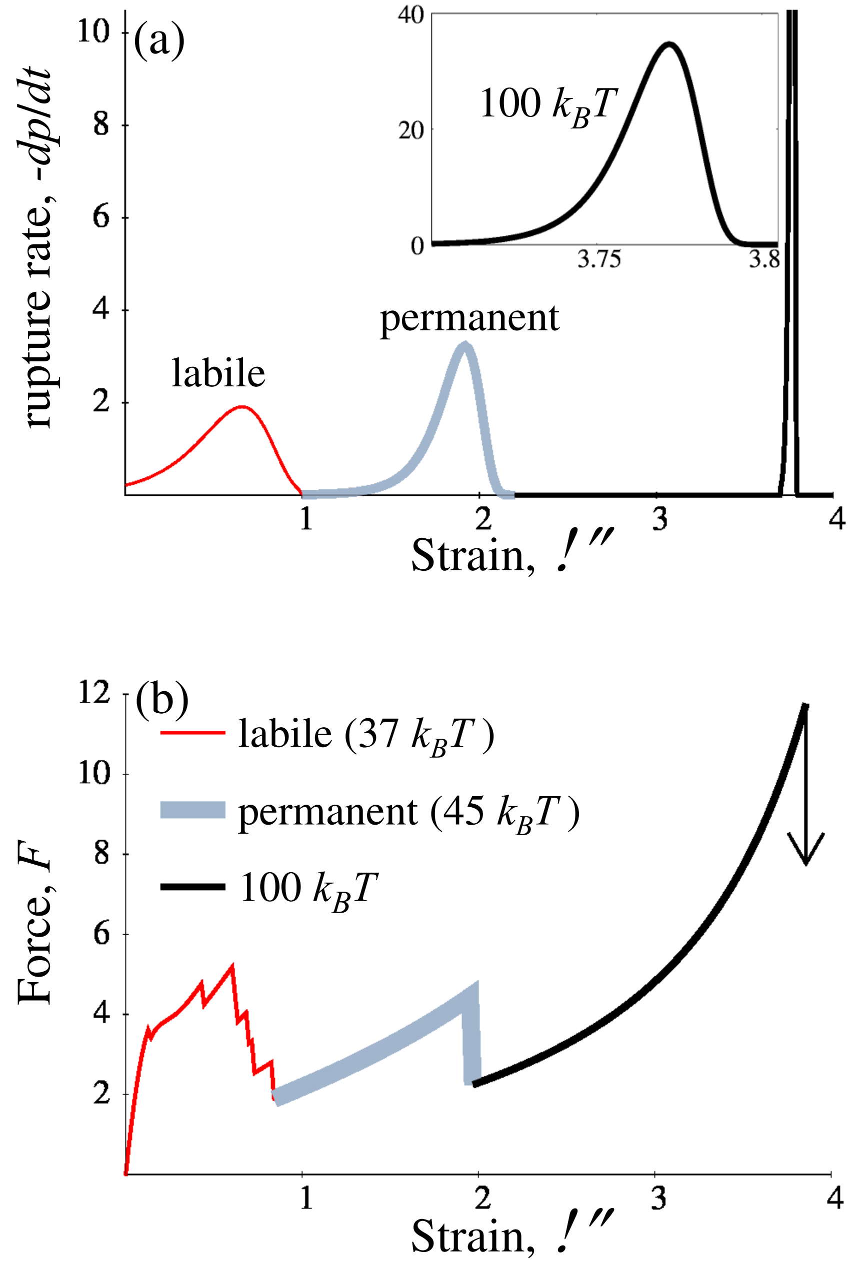
(a)
rupture rate, -dp/dt
10
8
6
4
2
labile
permanent
100 k_BT
40
20
0
3.75
3.8
1
2
3
4
Strain, !″
(b)
Force, F
12
10
8
6
4
2
labile (37 k_BT)
permanent (45 k_BT)
100 k_BT
1
2
3
4
Strain, !″

Fig. 4.

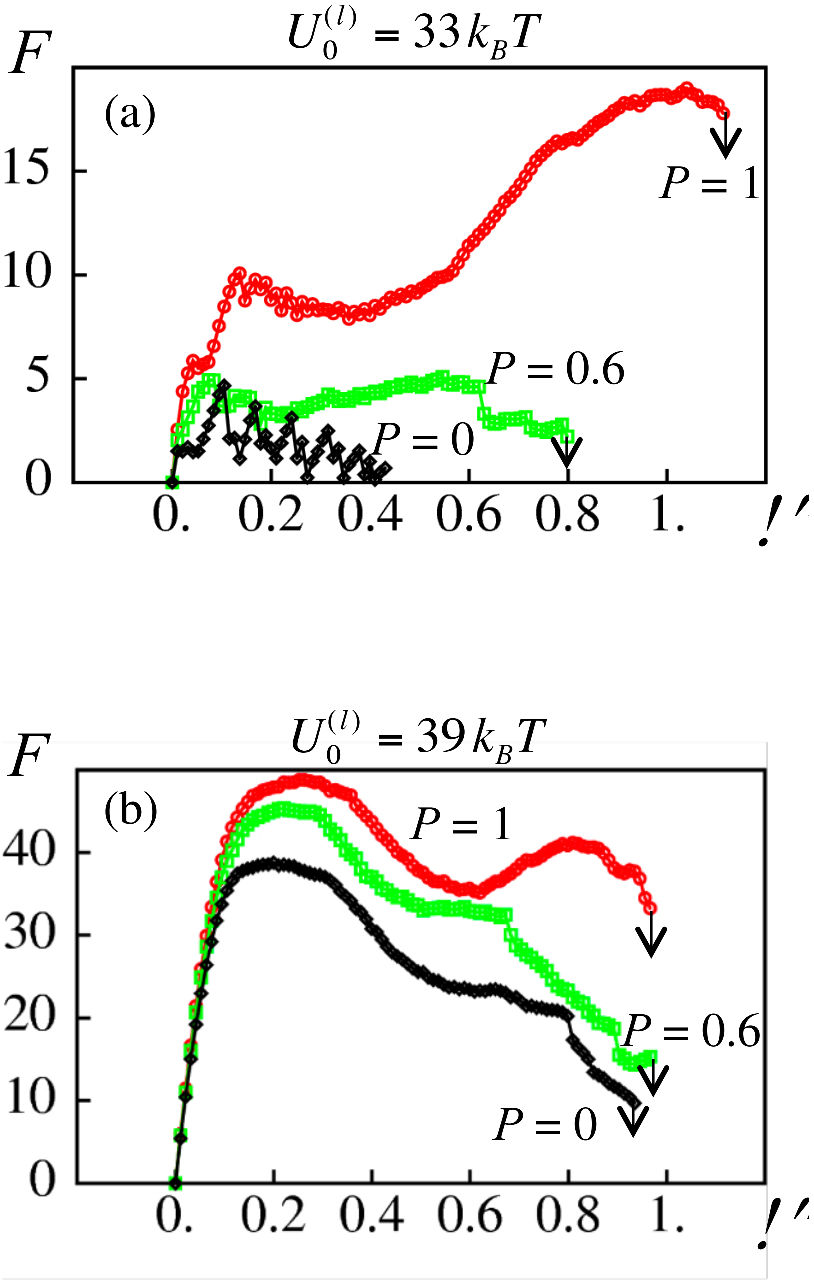
$U_0^{(l)} = 33\,k_BT$
F
(a)
15
10
5
0
0.
0.2
0.4
0.6
0.8
1.
!′
P = 1
P = 0.6
P = 0
$U_0^{(l)} = 39\,k_BT$
F
(b)
40
30
20
10
0
0.
0.2
0.4
0.6
0.8
1.
!′
P = 1
P = 0.6
P = 0

Fig. 5.

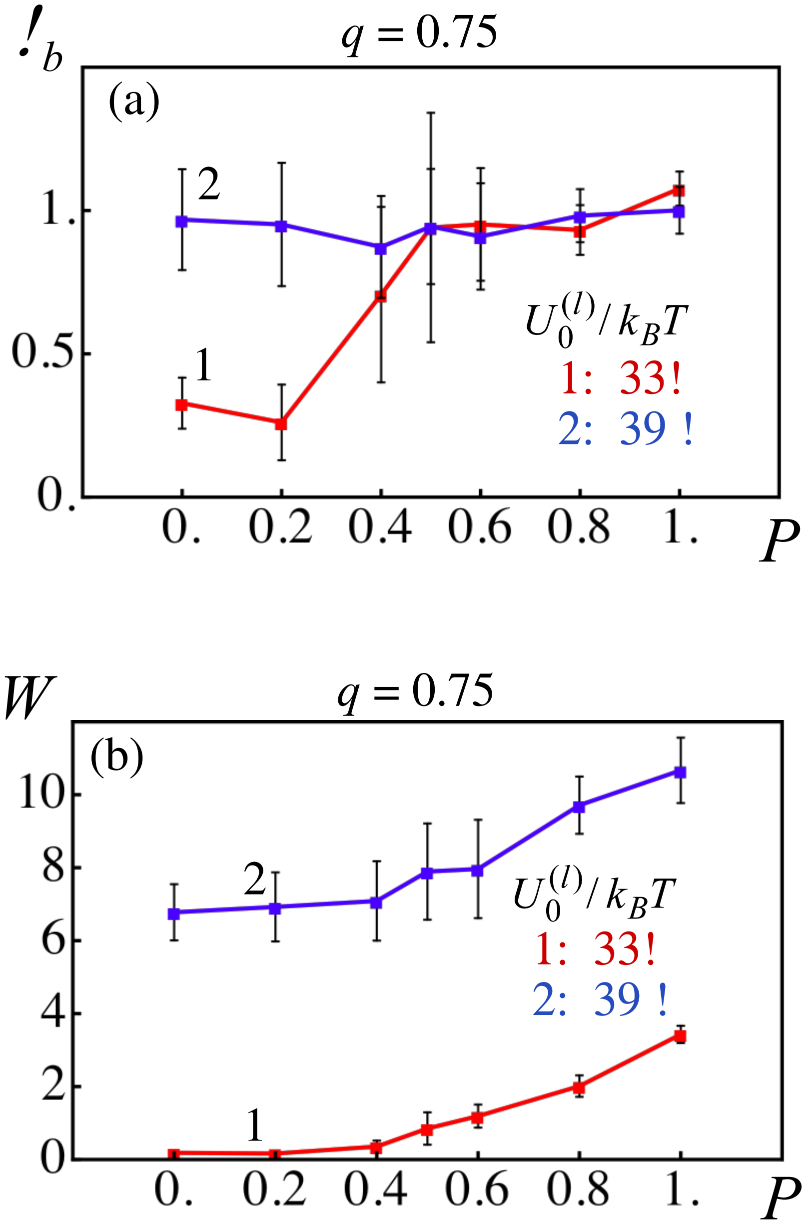
!_b
q = 0.75
(a)
1.
0.5
0.
0.
0.2
0.4
0.6
0.8
1.
P
2
1
U_0^(l) / k_B T
1: 33!
2: 39 !
W
q = 0.75
(b)
10
8
6
4
2
0
0.
0.2
0.4
0.6
0.8
1.
P
2
1
U_0^(l) / k_B T
1: 33!
2: 39 !

Fig. 6.

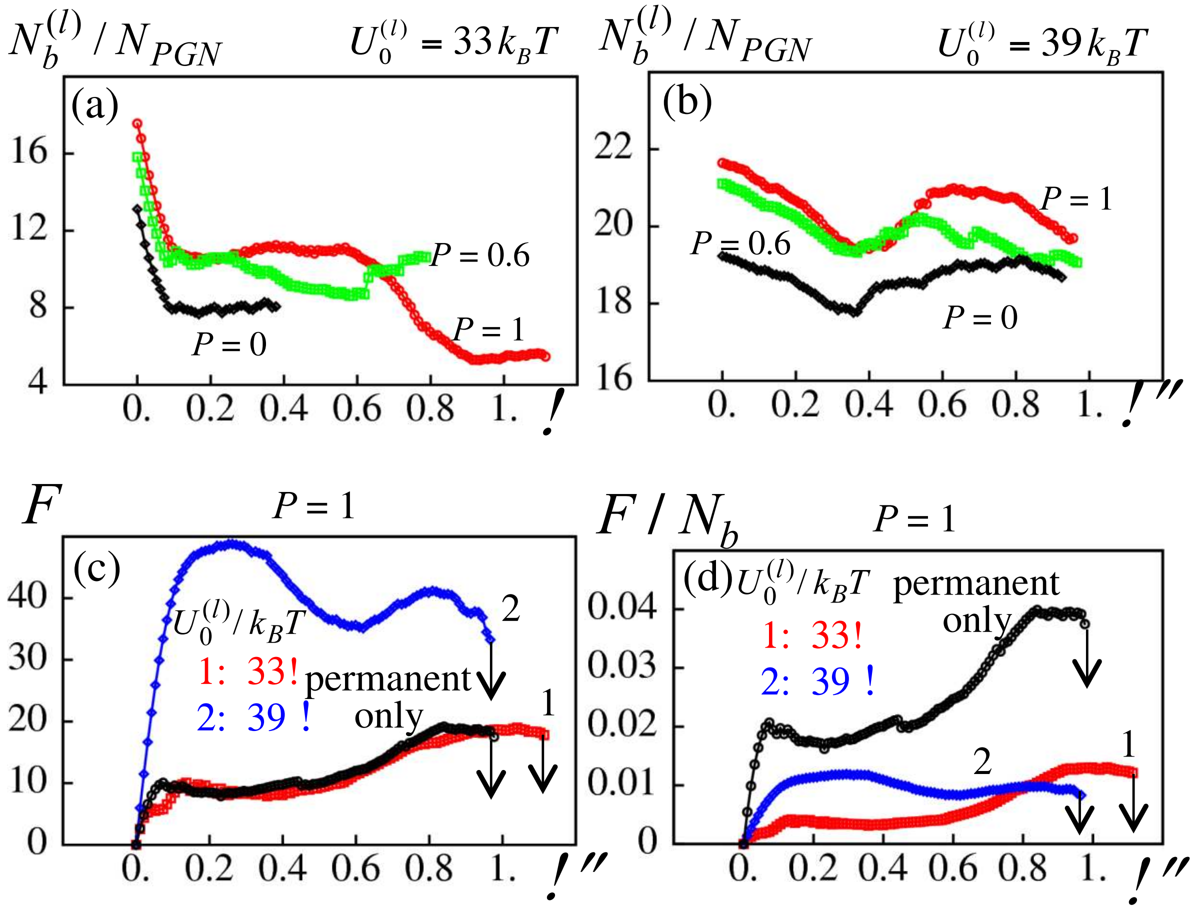
$N_b^{(l)} / N_{PGN}$
$U_0^{(l)} = 33 k_B T$
(a)
16
12
8
4
$P = 0.6$
$P = 1$
$P = 0$
0. 0.2 0.4 0.6 0.8 1.
!
$N_b^{(l)} / N_{PGN}$
$U_0^{(l)} = 39 k_B T$
(b)
22
20
18
16
$P = 1$
$P = 0.6$
$P = 0$
0. 0.2 0.4 0.6 0.8 1.
!″
F
$P = 1$
(c)
40
30
20
10
0
$U_0^{(l)} / k_B T$
1: 33!
2: 39 !
permanent only
2
1
0. 0.2 0.4 0.6 0.8 1.
!″
F / N_b
$P = 1$
(d) $U_0^{(l)} / k_B T$
permanent only
1: 33!
2: 39 !
0.04
0.03
0.02
0.01
0
2
1
0. 0.2 0.4 0.6 0.8 1.
!″

Fig. 7.

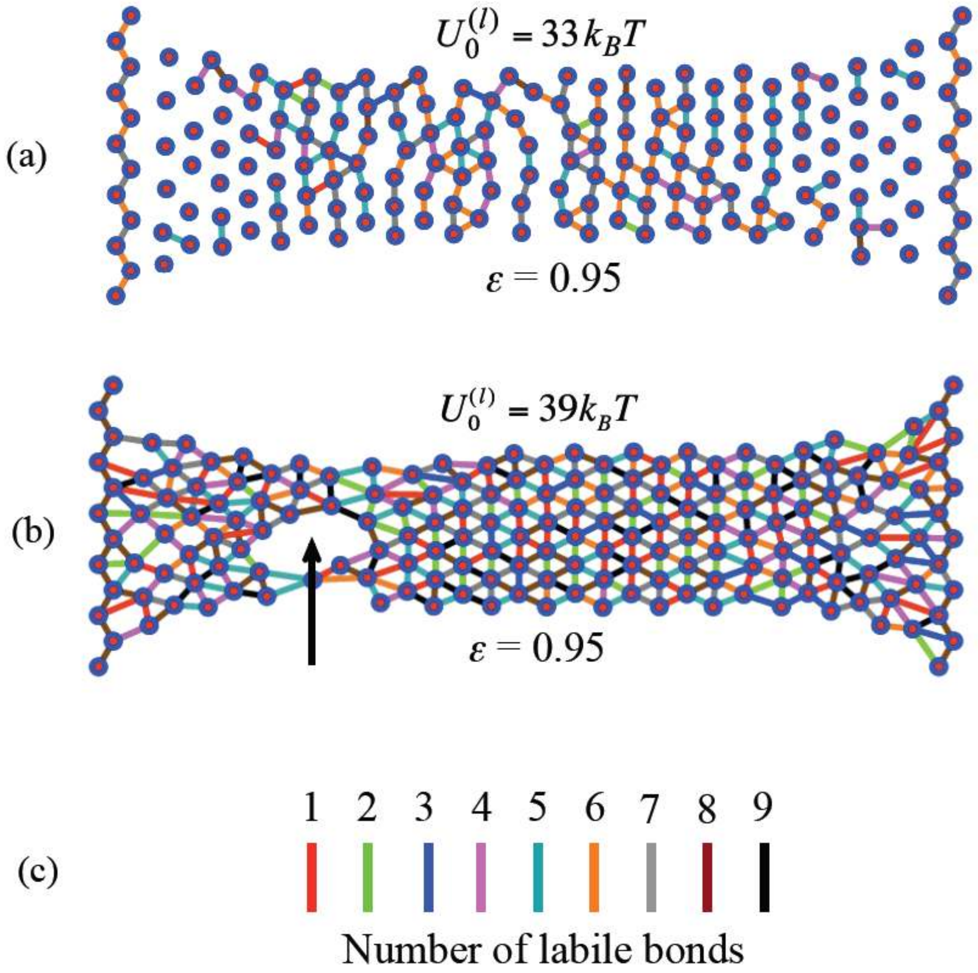
(a)
$U_0^{(l)} = 33k_BT$
$\varepsilon = 0.95$
(b)
$U_0^{(l)} = 39k_BT$
$\varepsilon = 0.95$
(c)
1 2 3 4 5 6 7 8 9
Number of labile bonds

Fig. 8.

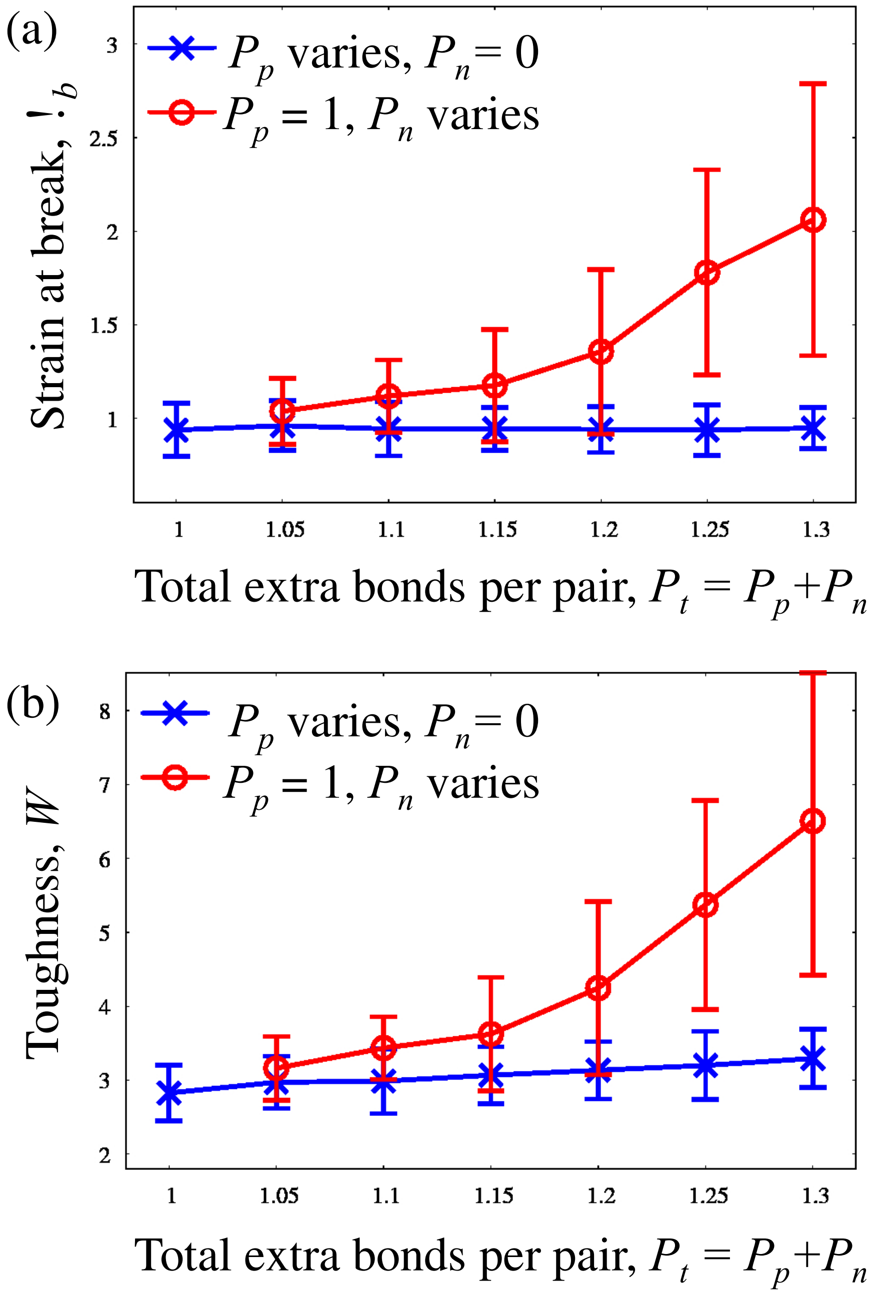
(a)
Strain at break, !·b
3
2.5
2
1.5
1
Pp varies, Pn = 0
Pp = 1, Pn varies
1
1.05
1.1
1.15
1.2
1.25
1.3
Total extra bonds per pair, Pt = Pp+Pn
(b)
Toughness, W
8
7
6
5
4
3
2
Pp varies, Pn = 0
Pp = 1, Pn varies
1
1.05
1.1
1.15
1.2
1.25
1.3
Total extra bonds per pair, Pt = Pp+Pn

Fig. 9.

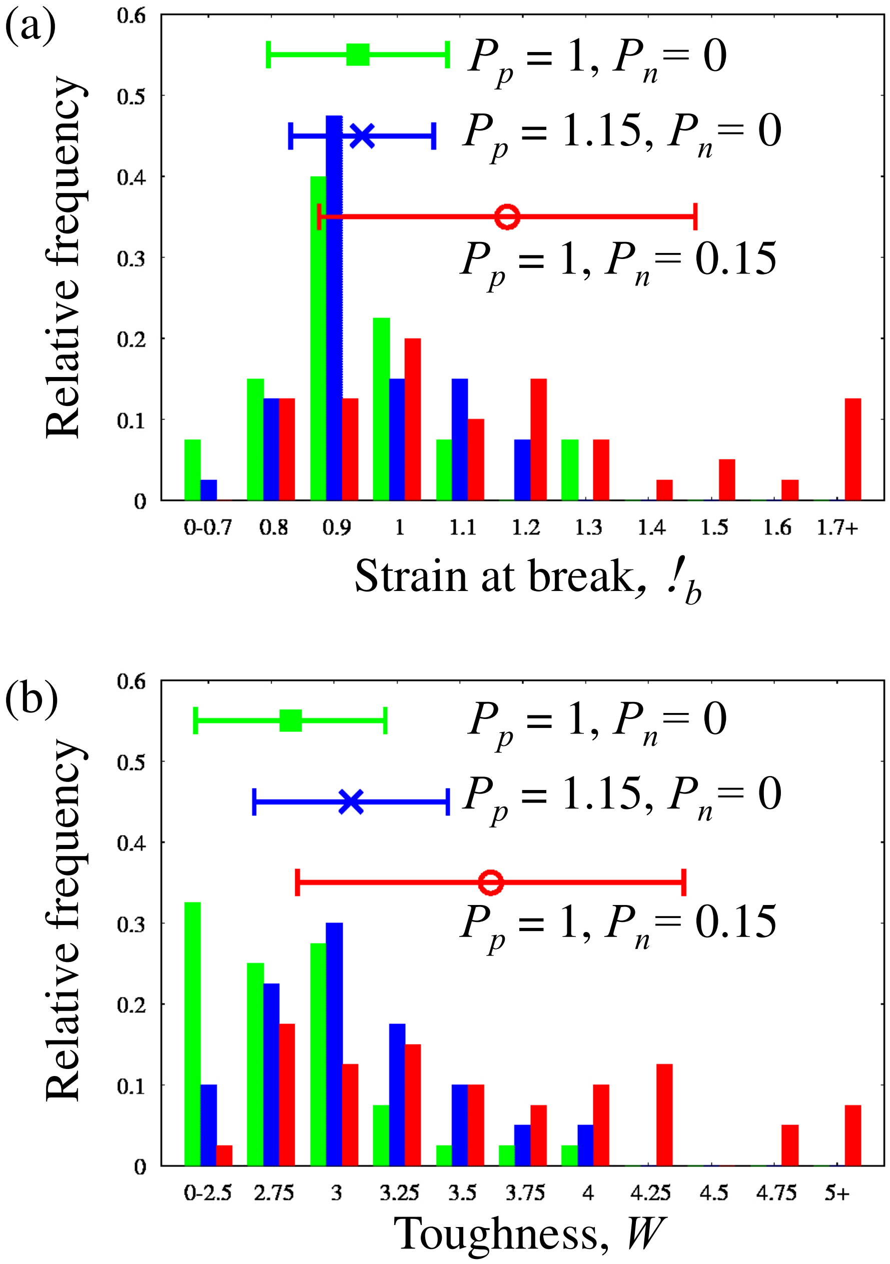
(a)
$P_p = 1, P_n = 0$
$P_p = 1.15, P_n = 0$
$P_p = 1, P_n = 0.15$
Relative frequency
0
0.1
0.2
0.3
0.4
0.5
0.6
0-0.7
0.8
0.9
1
1.1
1.2
1.3
1.4
1.5
1.6
1.7+
Strain at break, ε_b
(b)
$P_p = 1, P_n = 0$
$P_p = 1.15, P_n = 0$
$P_p = 1, P_n = 0.15$
Relative frequency
0
0.1
0.2
0.3
0.4
0.5
0.6
0-2.5
2.75
3
3.25
3.5
3.75
4
4.25
4.5
4.75
5+
Toughness, W

Fig. 10.

$P_p = 1, P_n = 0.15$

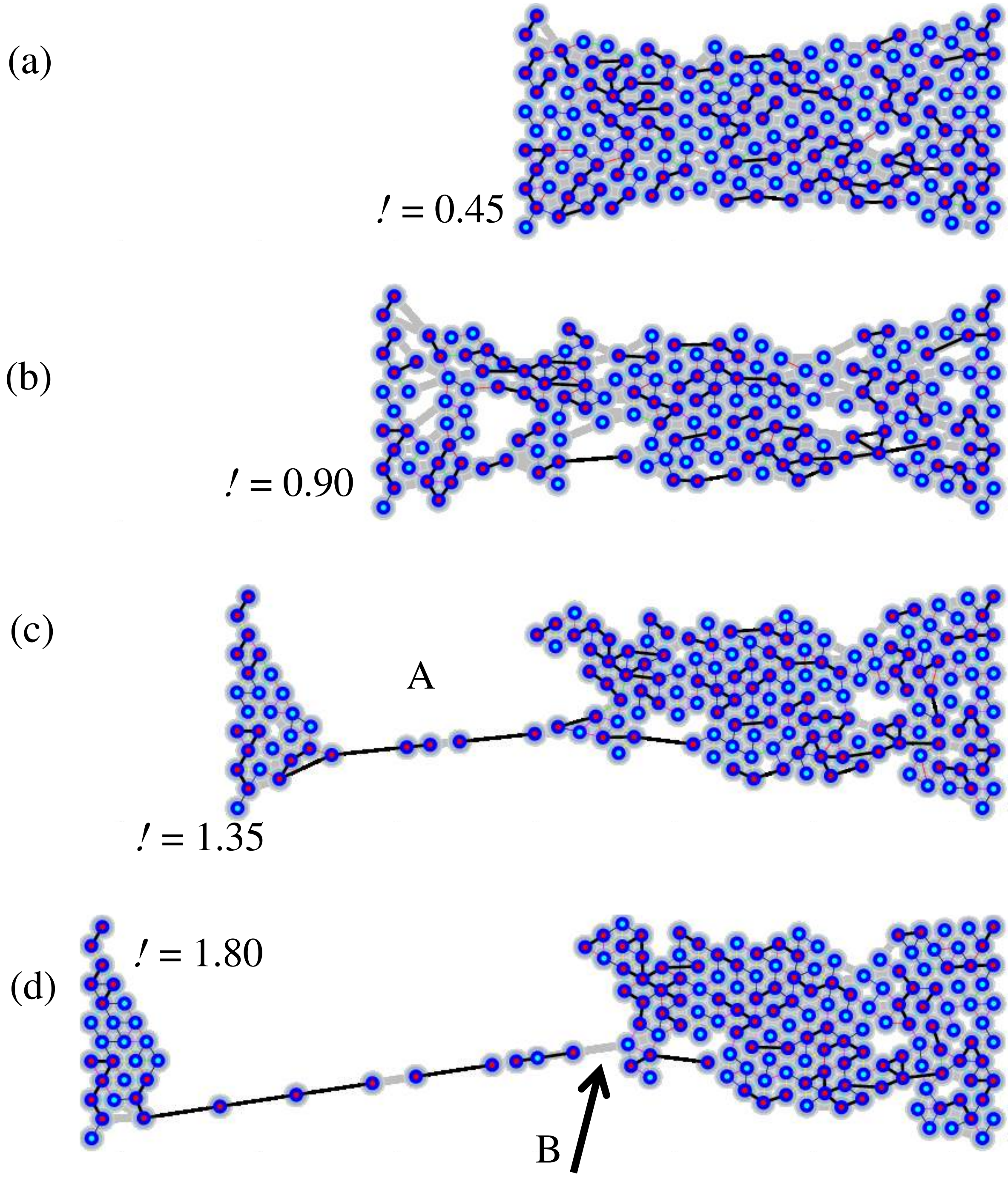

Fig. 11.

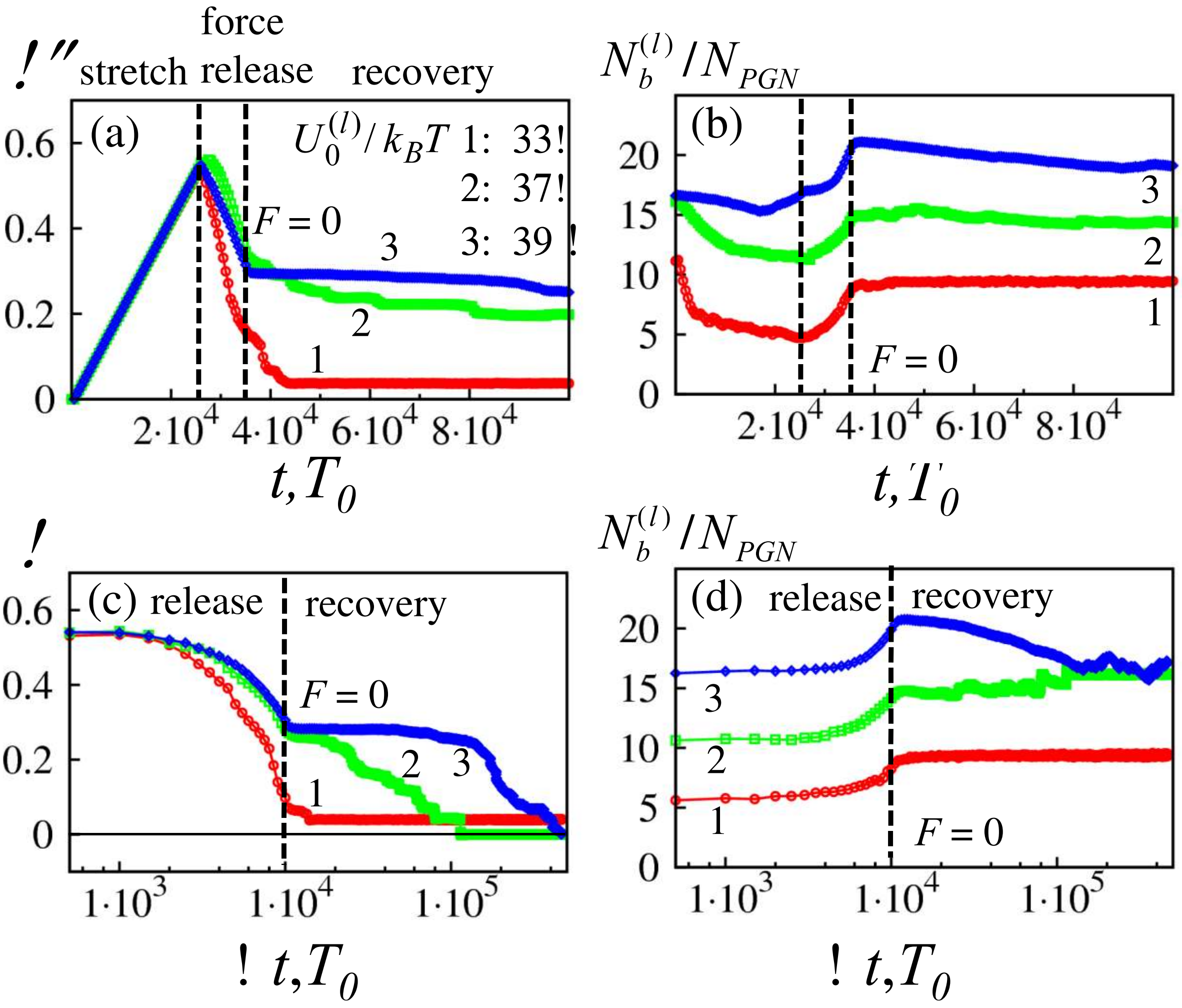
!″
stretch
force release
recovery
(a)
$U_0^{(l)}/k_BT$ 1: 33!
2: 37!
3: 39 !
$F = 0$
0.6
0.4
0.2
0
2·10⁴ 4·10⁴ 6·10⁴ 8·10⁴
t, T_0
$N_b^{(l)}/N_{PGN}$
(b)
20
15
10
5
0
t, T_0
!
(c) release
recovery
1·10³ 1·10⁴ 1·10⁵
! t, T_0
(d) release
recovery
1
2
3

Fig. 12.

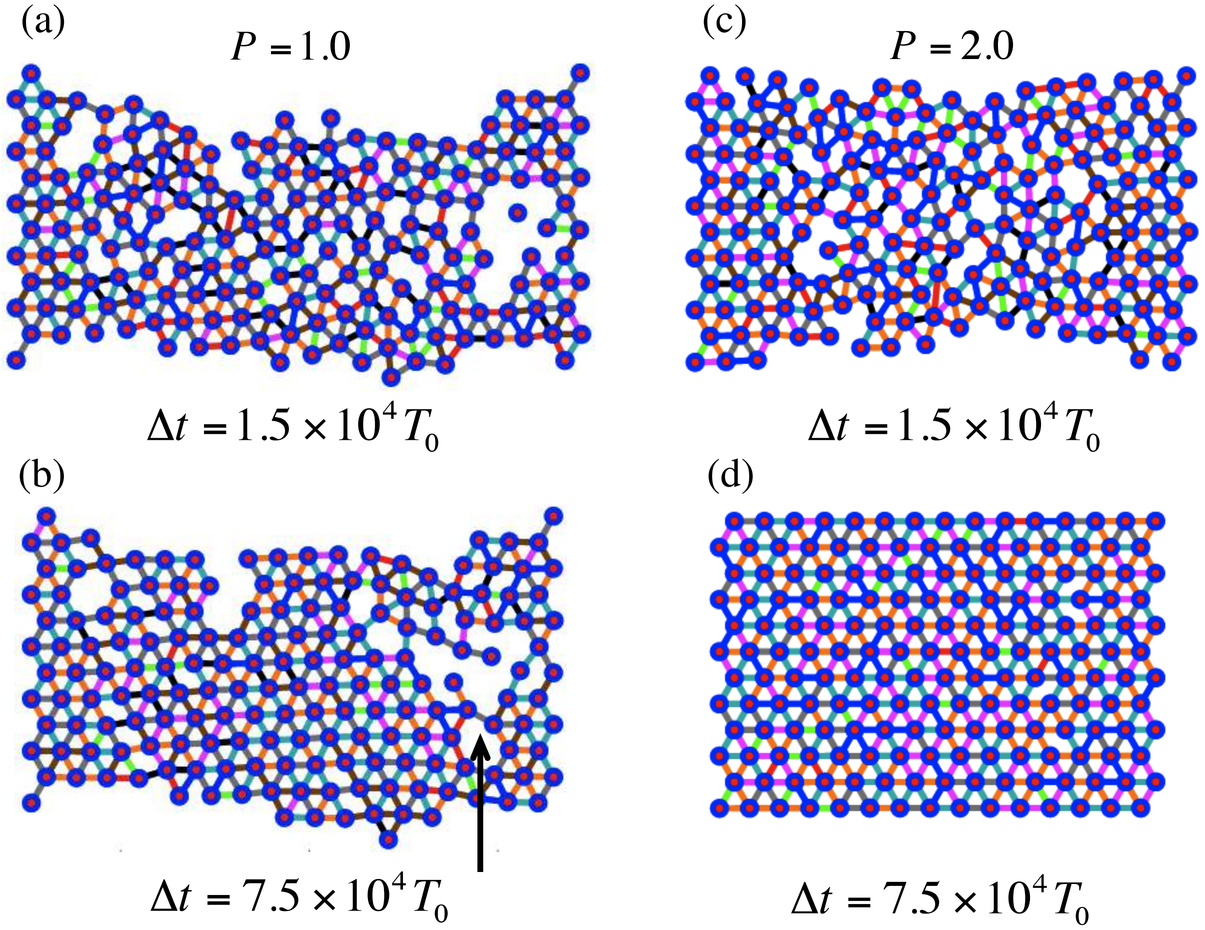
(a)
$P = 1.0$
$\Delta t = 1.5 \times 10^4 T_0$
(b)
$\Delta t = 7.5 \times 10^4 T_0$
(c)
$P = 2.0$
$\Delta t = 1.5 \times 10^4 T_0$
(d)
$\Delta t = 7.5 \times 10^4 T_0$

Fig. 13.

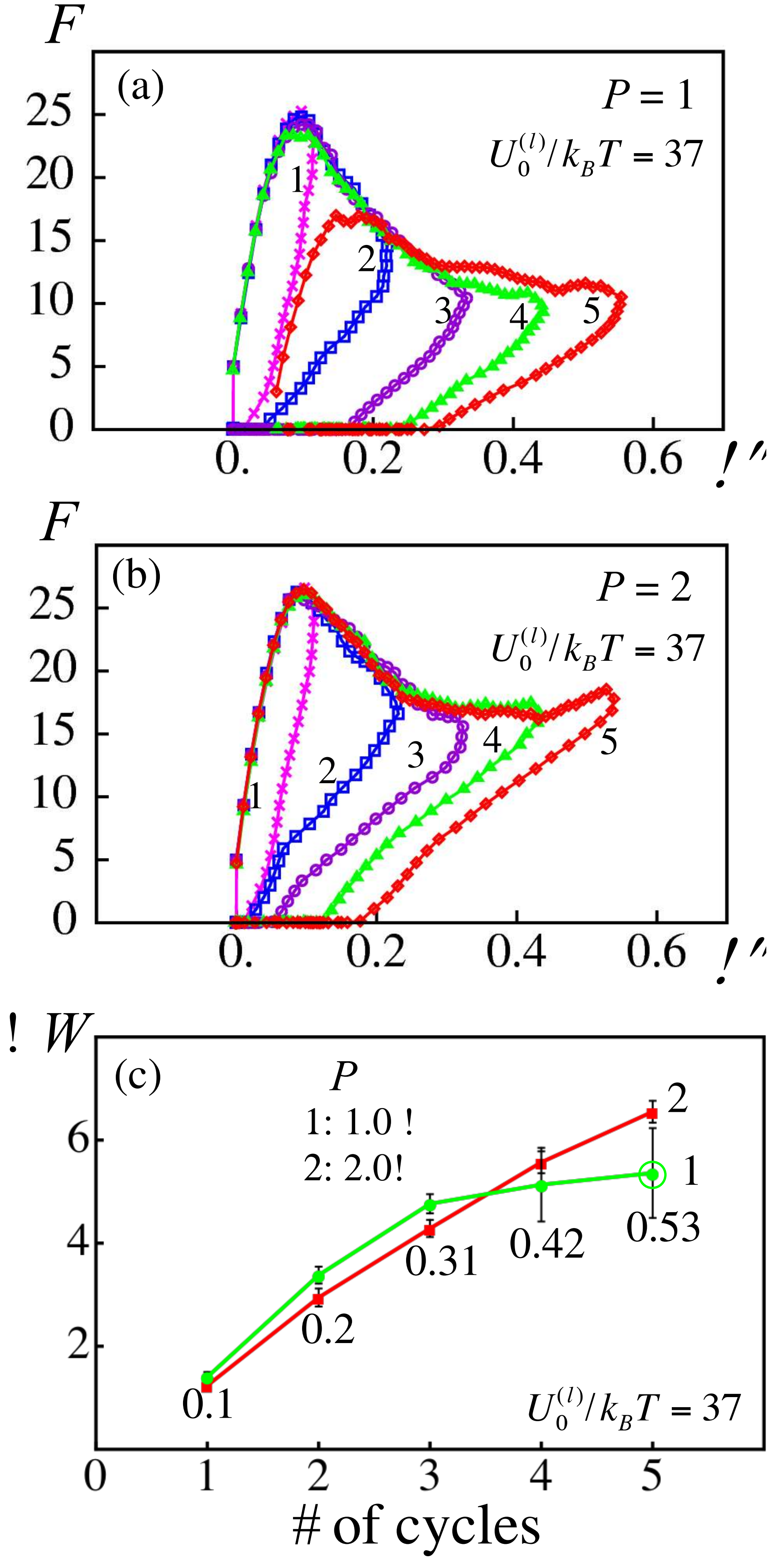
F
(a)
P = 1
$U_0^{(l)}/k_BT = 37$
25
20
15
10
5
0
0.
0.2
0.4
0.6
!′
1
2
3
4
5
F
(b)
P = 2
$U_0^{(l)}/k_BT = 37$
25
20
15
10
5
0
0.
0.2
0.4
0.6
!′
1
2
3
4
5
! W
(c)
P
1: 1.0 !
2: 2.0!
6
4
2
0
1
2
3
4
5
# of cycles
0.1
0.2
0.31
0.42
0.53
2
1
$U_0^{(l)}/k_BT = 37$

Table 1. Parameters used in the simulations

Dimensional units				
Length: nanoparticle radius	r_0 = 50 nm			
Time, t	T_0 = 1.41×10^{-2} s			
Velocity, v	$v_0 = r_0T_0^{-1}$ = 3.55 μm/s			
Force, F	F_0 = 2.98 pN			
Toughness, W	F_0r_0 = 89.74 kJ/mol			
Bond parameters	Weaker labile bond	Optimal labile bond	Stronger labile bond	Permanent bond
Bond energy, U_0	$33k_BT$	$37k_BT$	$39k_BT$	$45k_BT$
Rupture rate at F =0, k_{0r}	$6.55\times10^{-4}T_0^{-1}$	$1.2\times10^{-5}T_0^{-1}$	$1.62\times10^{-6}T_0^{-1}$	$4.03\times10^{-9}T_0^{-1}$
Formation rate, k_{0f}	$30T_0^{-1}$	$30T_0^{-1}$	$30T_0^{-1}$	0
Bond sensitivity, γ_0	$6\ F_0^{-1}$	$6\ F_0^{-1}$	$6\ F_0^{-1}$	$6\ F_0^{-1}$
Characteristics of polymer grafted nanoparticle (PGN)	Corona thickness $H=0.75r_0$		Corona thickness $H=1.25r_0$	
Kuhn length, l_p	1 nm			
Number of grafted arms, f	156			
Arm contour length, L	$8.89r_0$		$16.35r_0$	
Chain spring constant, κ_0	$7.81\times10^{-2}F_0r_0^{-1}$		$4.25\times10^{-2}F_0r_0^{-1}$	
Repulsion parameter	$3.02r_0$		$3.88r_0$	
Cohesion parameter A	1.15σ			
B	0.08σ			
C	$60k_BT$			
Mobility of PGN, μ	$0.57v_0F_0^{-1}$		$0.44v_0F_0^{-1}$	
Pulling velocity, v	$0.001v_0$ and $0.005v_0$			